Improved understanding of snowmelt runoff from the headwaters of China's Yangtze River using remotely sensed snow products and hydrological modeling

Pengfei Han[a], Di Long[a,*], Zhongying Han[a], Mingda Du[a], Liyun Dai[b], Xiaohua Hao[b]

[a] State Key Laboratory of Hydroscience and Engineering, Department of Hydraulic Engineering, Beijing 100084, China
[b] Northwest Institute of Eco-Environment and Resources, Chinese Academy of Sciences, Lanzhou 730000, China

ARTICLE INFO

ABSTRACT

As a crucial source of runoff in headwater regions, seasonal snowmelt plays an important role in ensuring water availability downstream, particularly during low flow periods. As the major constituent of China's water towers, the headwater region of the Yangtze River (HRYR) provides water to hundreds of millions of people downstream. Therefore, accurately simulating snowmelt is critical to developing a better understanding of the hydrological processes, which would, in turn, benefit water supply management, irrigation, hydropower generation, and ecological integrity over the HRYR and its lower reaches. However, it is a considerable challenge to conduct hydrological modeling for ungauged and poorly gauged headwater regions, owing to a lack of in situ measurements to appropriately constrain the model and evaluate its results. Satellite remote sensing provides an unprecedented opportunity to capture hydrological state variables globally, such as snow cover area (SCA) based on optical remote sensing and snow water equivalent (SWE) based on passive microwave remote sensing. This study simulates snow and glacier meltwater of the HRYR (above the Zhimenda gauging station), and quantifies proportional meltwater contributions to total runoff using multisource remote sensing data and a distributed hydrological model. We, for the first time ever, evaluate the snowmelt simulations based on the hydrological consistency among precipitation, air and land surface temperatures, and remotely sensed SWE/SCA. Results show that the snowmelt simulations using either SWE or SCA as a reference for calibrating parameters of the hydrological model are highly consistent, with snow and glacier meltwater contributing ~7% and ~5%, respectively, to the total runoff during 2003–2014. This study serves as a basis to simulate snowmelt to understand runoff generation and evolution under climate change across ungauged and poorly gauged headwater regions using multisource remote sensing data.

1. Introduction

Serving as water towers, mountains are important in providing water to hundreds of millions of people living downstream (Immerzeel, 2008; Viviroli and Weingartner, 2004). In headwater regions, snow and glacier meltwater is often the main source of runoff and plays an important role in ensuring water availability downstream (Barnett et al., 2005; Immerzeel et al., 2009; Immerzeel et al., 2010). Snow and ice reserves in headwater regions are sensitive to climate change (Immerzeel et al., 2010; Latif et al., 2018; Romshoo et al., 2015), which may result in hazards, such as spring flooding and bursts of glacier meltwater-fed lakes (Arnell and Gosling, 2016; Chen et al., 2017a; Chen et al., 2018; Palmer, 2017). According to the Fifth Assessment Report of the Intergovernmental Panel on Climate Change (IPCC), the global

mean surface temperature exhibited a warming trend of 0.85 °C (0.65 to 1.06 °C) from 1980 to 2012 (Pachauri et al., 2014). In particular, the annual mean near-surface air temperature increased by 1.8 °C during 1961–2007 based on observations from 90 weather stations across Tibet (Wang et al., 2008). Accurately observing or simulating snow/glacier meltwater is of high importance for understanding hydrological processes in high mountain regions, reducing flooding hazards induced by meltwater, managing water supplies, and conserving water resources and ecosystems in headwaters and downstream.

Capturing variations in precipitation, air and land surface temperatures (LST), and snow with topography is a prerequisite for a better understanding and simulation of hydrological processes in such regions (Chen et al., 2018; Henn et al., 2018; Lundquist et al., 2018; Tang et al., 2018b). However, high mountain areas are typically poorly gauged and
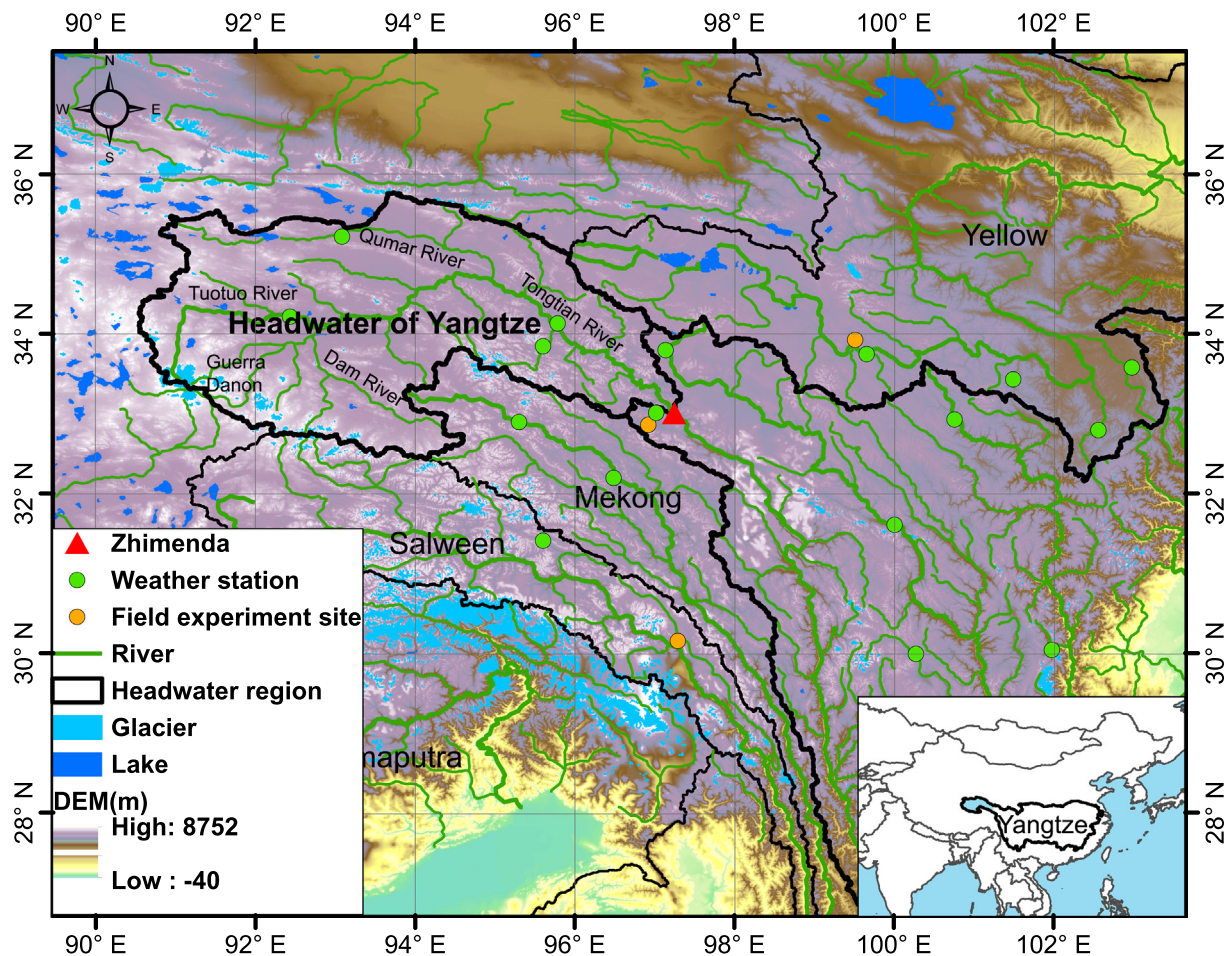
Fig. 1. Location of the headwater region of the Yangtze River (HRYR), gauging station (Zhimenda), weather stations, field sites, glaciers, lakes, and elevations.

inaccessible, owing to harsh environments and complex terrain. This leads to difficulties in understanding hydrological processes owing to relatively large uncertainties in the forcing data of models and a lack of in situ measurements to appropriately evaluate simulations. Other than inaccessibility, accuracy is another significant problem. Over high mountain regions, in situ measurements, if any, are typically collected in valleys and therefore, cannot be used to represent gradients of precipitation, air temperature, and LST. In general, the accuracy of measured hydrological variables is lower in mountainous terrain than it is in flat terrain. Taking precipitation as an example, measurement errors, e.g., undetected rainfall or snowfall by a gauge, could lead to marked deviations in simulations (Hay et al., 2002; Tang et al., 2017). Large slopes and strong winds also affect the catches of precipitation gauges and generate systematic errors in precipitation measurements (Klemes, 1990). Therefore, it is challenging to develop a reliable understanding of hydrological processes over high mountain regions only based on in situ measurements. Satellite remote sensing provides an unprecedented opportunity for capturing valuable information on hydrological state and flux variables [e.g., precipitation, snow cover area (SCA), snow water equivalent (SWE), and total water storage (TWS) change], as well as land surface state and properties (e.g., LST and surface albedo), which are particularly important for improving hydrological model predictions (Famiglietti et al., 2015; Huang et al., 2018a, 2018b; Long et al., 2014; Long et al., 2015; Long et al., 2016; Pietroniro and Prowse, 2002; Schmugge et al., 2002). Therefore, remote sensing data are favorable for hydrological modeling in high mountain regions, as their resolutions and availability do not depend on terrain characteristics (Parajka and Blöschl, 2008). Joint use of remote sensing data and limited in situ measurements could develop a better understanding of

hydrological processes, in particular generation of snow and glacier meltwater in mountainous terrain.

Considering the importance of snow and glacier meltwater in water supply and domestic usage downstream, evaluation of meltwater simulations is required in order to perform reliable simulations of hydrological processes (Immerzeel et al., 2010; Sorg et al., 2012). Evaluations of meltwater simulations based on in situ measurements are lacking; instead, many studies have evaluated melting processes by comparison with simulated SCA, SWE, or glacier area changes using satellite-based retrievals (Dressler et al., 2006; Ferguson, 1999; Shrestha et al., 2015; Zappa et al., 2003; S. Zhang et al., 2012). Nevertheless, these studies evaluated melting processes with a single dataset such as SCA or SWE, which may lead to uncertainties and deviations in simulation results. An effective method of evaluating meltwater simulations for ungauged and poorly gauged headwater regions is based on the hydrological consistency (EHC), which is similar to methods employed for qualitatively evaluating evapotranspiration (McCabe et al., 2008). If the simulated snowmelt from different calibration references exhibits high consistency, the proportional contribution of the snowmelt to total runoff should be close and regarded as reliable. The EHC can be measured by the ratio of snowmelt contributions to total runoff with either SWE or SCA as the calibration reference. If the ratio is close to 1, the simulated snow meltwater is more reliable.

The overall objective of this study was to introduce a method to evaluate meltwater simulations and enhance the understanding of snow and glacier meltwater by quantifying their proportional contributions to the total basin discharge of the headwater region of the Yangtze River (HRYR, above the Zhimenda gauging station and one of China's
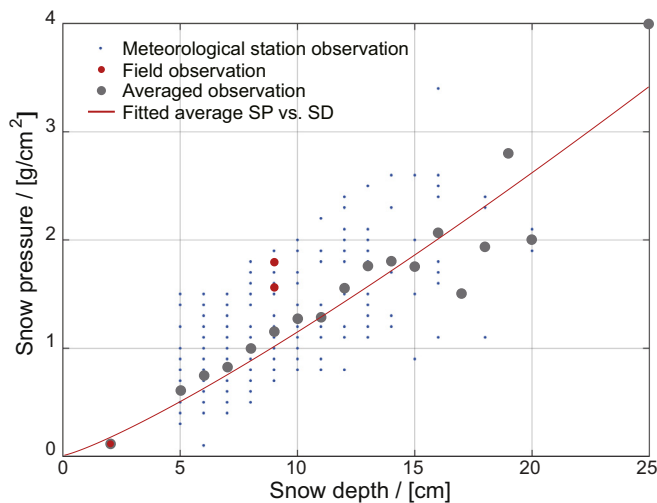
Fig. 2. Relationships between snow depth and snow pressure; small blue points denote observations from meteorological stations, red points observations from field experimentation, and grey points average *SP* for a specific *SD*. The red curve provides a plotting of (Eq. (1)). (For interpretation of the references to colour in this figure legend, the reader is referred to the web version of this article.)

most important water sources) using multisource remote sensing data and the Coupled Routing and Excess STorage model (CREST; Shen et al., 2016; Wang et al., 2011; Xue et al., 2013), coupled with a snow and glacier melt module (Chen et al., 2017b; hereafter referred to as CREST-snow). To achieve this objective, this study involves: (1) simulating snowmelt using either remotely sensed SCA or SWE as the calibration reference in CREST-snow and evaluating snowmelt simulations based on EHC; and (2) quantifying the proportional contributions of snow and glacier meltwater to the total basin discharge for the HRYR. This study serves as a basis for simulating snowmelt to understand runoff generation and evolution under climate change across ungauged and poorly gauged high mountain regions. The results of this study have important implications for improving water resource management and ecosystem protection for the HRYR and its downstream regions.

2. Study area and data

2.1. Study area

The HRYR, with a drainage area of ~139,000 km^2 accounting for ~8% of the area of the Yangtze River basin, is located in the hinterland of the Qinghai-Tibetan Plateau (roughly ranging between 90°30′–97°18′E and 32°24′–35°46′N). With elevations ranging from 3500 to 6400 m and a mean elevation of 4670 m, this is among the highest basins in the world (Fig. 1). The headwaters consist of three major tributaries, i.e., (1) the Qumar River in the north, originating from the southern piedmont of the eastern section of the Kunlun Mountains; (2) the Tuotuo River in the west, originating from the Guerra Danon glaciers in the Tanggula Mountains; and (3) the Dam River in the south, originating from marshes on the piedmont of the eastern section of the Tanggula Mountains. These tributaries converge into the mainstream (the Tongtian River) and form a fan-shaped structural network (Sun et al., 1992). The Zhimenda gauging station is located in Yushu Tibetan Autonomous Prefecture of Qinghai Province, and is associated with relatively complete and long-term flow discharge measurements. The glacierized area is about 1400 km^2 according to the second Chinese glacier inventory (Guo et al., 2015; Wei et al., 2014), accounting for ~1% of the HRYR and feeding a variety of ecosystems on the plateau.

The HRYR has a typical alpine climate, with intense sunshine and

diurnal temperature changes. The location of the headwater region and topographical characteristics of the Tibetan Plateau (hereafter referred to as TP) result in a subhumid to semi-arid climate. During 2003–2014, the annual precipitation of the HRYR ranged from 360 to 590 mm, with a mean annual precipitation of 475 mm, based on the China Gauge-based Daily Precipitation Analysis (CGDPA) product (Shen and Xiong, 2016). Precipitation over the HRYR exhibits an increasing trend, resulting in an increased runoff as the primary factor governing long-term discharge (Wang et al., 2017). Snow cover area in the HRYR in all seasons except for the summer during 2003–2014 accounted for ~10% of total study area based on the MODerate resolution Imaging Spectroradiometer (MODIS) snow cover product (see Section 2.2.3), and showed an increasing trend from 2000 to 2012 due to warmer and wetter climate, which is important given its variability that largely influences regional runoff dynamics (Wang et al., 2015). Under global warming, the temperature in this region has exhibited a rising trend of 0.07–0.23 °C per decade during 1967–2007 (Wang et al., 2007). It is expected that the mean minimum temperature will increase by 1.1 °C in the 2020's (Li et al., 2012). The environment in the headwaters is cold, owing to the high elevation. During 2003–2014, the annual mean LST ranged from −4.8 to −2.2 °C with a mean annual temperature of −3.0 °C, based on the LST products from MODIS.

2.2. Data and processing

2.2.1. Field experiment and in situ measurements

In situ measurements of snow depth (*SD*) and snow pressure (*SP*) were employed in this study. These are highly valuable for determining a more reasonable SWE for snowmelt simulation. The in situ measurements were obtained from 17 meteorological stations from across the Upper Yangtze River basin and its surrounding areas during 2003–2008. In addition, we carried out a field investigation using a snow fork, spectrograph, thermometer, and other necessary instruments during the 17 Feb to 7 Mar, 2017 period to describe the characteristics of the snow across the TP (Fig. 2). Measured snow depths and snow pressure were used to develop a functional relationship between the two variables, so that the passive microwave (hereafter referred as PMW) remote sensing-derived snow depths may be used to estimate SWE for model calibration. For a given snow depth, the snow pressure was determined by multiple factors, such as seasonality, age of the snow, relative humidity, and temperature (USACE, 1956; McKay and Thompson, 1968; Seligman and Douglas, 1936). The average snow pressure at a specific snow depth was determined as follows:

$$SP = 0.0735 \times SD^{1.193}, \tag{1}$$

where *SP* denotes the snow pressure and *SD*, the snow depth (Fig. 2).

Along with in situ measurements, multisource remote sensing data (i.e., precipitation, SWE, SCA, temperature, and other ancillary data) were also used in forcing the model or used as calibration references.

2.2.2. Precipitation

In this study, six daily precipitation data sources were compared: (1) one rain gauge-based product (CGDPA); (2) one reanalysis product (ERA-Interim); and (3) four satellite-based precipitation products (i.e., GSMaP, PERSIANN-CDR, TRMM 3B42V7, and CMORPH-CRT). The CGDPA precipitation product is at a quarter degree resolution, incorporating precipitation measurements from ~2400 gauges across mainland China, measured since 1955 (Shen and Xiong, 2016). The ERA-Interim reanalysis precipitation product is spatially and temporally complete, with a quarter degree spatial resolution (Lindsay et al., 2014). The satellite-based precipitation products with a quarter degree resolution included: (1) the Tropical Rainfall Measuring Mission (TRMM) 3B42V7 product between 50°N and 50°S (Huffman et al., 2007), (2) the Global Satellite Mapping of Precipitation (GSMaP) Gauge Reanalysis product for 2003–2014; (3) Precipitation Estimation from Remotely Sensed Information Using Artificial Neural Networks–Climate

Data Record (PERSIANN-CDR) between 60°N and 60°S incorporating measurements since 1983 (Ashouri et al., 2015), and (4) the Climate Prediction Center morphing method bias-corrected version (CMORPH-CRT) precipitation estimate (Joyce et al., 2004). The precipitation product that was most suited to the study area, i.e., CGDPA, was used as input in CREST-snow. A detailed description of precipitation products can be found in Section 1 of the Supporting Information.

2.2.3. Snow water equivalent and snow cover area

SCA employed in this study was obtained from MODIS observations. The eight-day maximum SCA extent (MOD10A2 and MYD10A2) with a 500 m spatial resolution was employed, to reduce the influence of cloud cover (Hall et al., 2006, 2007). MOD10A2 was obtained from the Terra platform orbiting from north to south (descending node) with a morning equatorial crossing at 10:30 am (local time), and MYD10A2 was obtained from the Aqua platform orbiting from south to north (ascending node) with an afternoon equatorial crossing at 1:30 pm (local time). For the two datasets, if snow was observed on any day for the daily snow cover extent product, this was classified as snow cover in the eight-day composite. Hall and Riggs (2007) found that the overall absolute accuracy of the MODIS product was ~ 93%, and it was therefore adopted as a reliable calibration reference. To take full advantage of the two SCA sources, i.e., MOD10A2 and MYD10A2, the snow cover fraction was calculated as the intersection between the two products. In addition, MODIS SCA products and PMW SWE were resampled to 1 km × 1 km, in accordance with the other forcing variables.

SWE was derived from snow depth retrievals obtained from WestDC (Cold and Arid Regions Science Data Center at Lanzhou, http://westdc. westgis.ac.cn/). The raw data for generating the snow depth dataset was obtained from daily PMW brightness temperatures from the Scanning Multichannel Microwave Radiometer (SMMR), Special Sensor Microwave Imager (SSM/I), and Special Sensor Microwave Imager/Sounder (SSMI/S) sensors processed by the National Snow Ice Data Center (NSIDC; Che et al., 2008; Dai et al., 2015; Dai et al., 2012). Based on the relationship between snow pressure and snow depth [i.e., Eq. (1)], SWE may be calculated as follows:

$$\text{SWE} = \frac{\rho_{\text{snow}} \times SD}{\rho_{\text{water}}} = \frac{0.0735 \times SD^{1.193}}{\rho_{\text{water}}}, \tag{2}$$

where SD denotes the PMW-based snow depth and ρ_{water} the density of liquid water.

Dong et al. (2005) found that uncertainty in PMW SWE is associated with snow pack mass, distance to significant open water bodies, daytime air temperature, forest cover, snow class, and topographic roughness and aspect. The spatial resolution of PMW SWE is relatively coarse and may result in additional uncertainty. However, information on SWE is still valuable. SWE is an important hydrological state variable as it reflects the actual amount of water stored in snowpack. Snow cover information can only tell whether the land is covered by snow. In addition, optical remote sensing-based snow cover is subject to cloud contamination. PMW is currently the only efficient and practical way to monitor the spatiotemporal variability in snow depth at the regional scale. Incorporating information on remotely sensed snow cover and SWE is critical to snowmelt runoff simulation, despite the uncertainties in the two products.

2.2.4. Land surface and air temperatures

Two daily LST products were employed at a 1 km × 1 km spatial resolution, i.e., MOD11A1 and MYD11A1 from Terra and Aqua, respectively. Each product has two LST sets each for the daytime and nighttime portion of the day, and hence four LST sets were derived per day. The average LST can be calculated in order to reduce random error and represent the daily mean temperature. The MODIS LST products were reconstructed using a multi-temporal classification and robust

regression approach to remove cloud cover (Zeng et al., 2015). This method is practical but uncertainty still remains, and uncertainty in LST caused by cloud cover may affect snowmelt simulation to some degree. The daily near-surface air temperature dataset, developed by the National Meteorological Information Center, was generated from observations of ~2000 ground-based weather stations across mainland China using the thin-plate spline (TPS) method (Hutchinson, 1995). The dataset has a daily resolution and a spatial resolution of 0.5° × 0.5°, with observations since 1961. It includes daily maximum, minimum, and mean near-surface temperatures. In this study, the daily mean near-surface temperature was used. Mostovoy et al. (2006) found that MODIS LST can be employed to estimate daily air temperatures using linear regression. Combining these estimates can improve the quality and accuracy of the air temperature estimate produced by spatial interpolation from point-based observations. Therefore, we downscaled the near-surface air temperature to 1 km × 1 km using linear regression (Chen et al., 2017b; Neteler, 2010). A detailed description of this downscaling approach can be found in Section 2 of the Supporting Information.

2.2.5. Ancillary datasets

The topographical information of the study area, i.e., a digital elevation model (DEM) with a spatial resolution of 1 km × 1 km, was downloaded from HydroSHEDS (https://hydrosheds.cr.usgs.gov/), a mapping product derived from NASA's Shuttle Radar Topography Mission (SRTM; Hensley et al., 2000). Daily discharge data from the Zhimenda gauging station from 2003 to 2014 were employed for the total runoff simulation with CREST-snow.

3. Methodology

3.1. Model

The Coupled Routing and Excess STorage model (CREST) is a distributed hydrological model jointly developed by the University of Oklahoma and NASA SERVIR (Shen et al., 2016; Wang et al., 2011; Xue et al., 2013). Previous studies have demonstrated that the model performs well in simulating runoff, even across poorly gauged basins (Khan et al., 2010; Khan et al., 2011; Wang et al., 2011; Xue et al., 2013; Zhang et al., 2015). The study regions have been mainly concentrated in tropical or snow-free regions without considering snow and glacier melt processes in runoff simulation. To apply to cryospheric or high mountain regions, where snow and glacier melting plays a significant role, the CREST model needs to be coupled with a snow and glacier melt module to better simulate the total runoff and its components. This study employed a temperature index-based snowmelt module coupled with CREST (Chen et al., 2017b) to simulate hydrological processes for the HRYR. Parameters for snowmelt simulation are provided in Table 1.

Precipitation is partitioned into solid and liquid components according to the following temperature criterion:

$$P_s = \begin{cases} 0 & \frac{T_{\text{lst}} + T_{\text{air}}}{2} \geq T_r \\ \left(\frac{\left(\frac{T_{\text{lst}} + T_{\text{air}}}{2} \right) - T_s}{T_r - T_s} \right) \cdot P_{\text{tot}} & T_s < \frac{T_{\text{lst}} + T_{\text{air}}}{2} < T_r, \\ P_{\text{tot}} & \frac{T_{\text{lst}} + T_{\text{air}}}{2} \leq T_s \end{cases} \tag{3}$$

where P_s and P_{tot} are the solid and total precipitation, respectively; T_r and T_s are the temperature thresholds for rainfall and snowfall, respectively, which are calibrated using the snowmelt module and remotely sensed SWE or SCA; T_{lst} is the daily mean LST derived by four LST observations; and T_{air} is the daily mean near-surface air temperature obtained from the China Meteorological Administration and downscaled by LST using linear regression (Chen et al., 2017b; Neteler,

Table 1
Parameters of the snowmelt simulation and their values in this study.

Parameter	Description	Value	Unit	Lower bound	Upper bound	Calibration reference
T_s	Snowfall temperature threshold	$-3.5/-4.0$	°C	-6	3	SWE/SCA
T_r	Rainfall temperature threshold	$-2.1/-2.1$	°C	-6	3	SWE/SCA
$T_{s,mlt}$	Snowmelt temperature threshold	$-4.6/-1.4$	°C	-6	3	SWE/SCA
$d_{s,mlt6}$	Max. snowmelt factor	10.2/8.7	mm °C^{-1} d^{-1}	0	12	SWE/SCA
$d_{s,mlt12}$	Min. snowmelt factor	5.7/4.5	mm °C^{-1} d^{-1}	0	10	SWE/SCA
SFSWE	Reference depth of snow sublimation	9.5	mm	9	20	SWE
SFSCA	Percentage of snow after sublimation	0.92	–	0	1	SCA
Swe2ScaTh	Threshold of translating SWE to SCA	5.8	mm	3	20	SCA

2010).

3.1.1. Snowmelt simulation using snow water equivalent as reference

In the case of calibration with SWE, the simulated SWE at the tth time period (SWE_t) is updated based on the mass conservation, with a default SWE of zero on the first day:

$$SWE_{t+1} = SWE_t - SM_t + P_{s,t} \cdot Factor_t \tag{4}$$

where $P_{s,t}$ is the solid precipitation at the tth time period; SWE_t is the SWE at the tth time period; $Factor_t$ is a variable to take into account snow sublimation; and SM_t is the snowmelt at the tth time period, i.e.,

$$SM_t = min\{S_{t,mlt}, SWE_t\}, \tag{5}$$

where $S_{t,mlt}$ is the potential snowmelt at the tth time period, which is calculated using a degree-day factor (DDF_{snow}, see below), i.e.,

$$S_{s,mlt} = DDF_{snow}\left(\frac{T_{lst} + T_{air}}{2} - T_{s,mlt}\right)\Delta t, \tag{6}$$

where Δt is a daily timestep. The degree-day factor, DDF_{snow}, is calculated from an application of a sinusoidal equation, or more precisely

$$DDF_{snow} = \frac{d_{s,mlt6} + d_{s,mlt12}}{2} + \frac{d_{s,mlt6} - d_{s,mlt12}}{2} \cdot \sin\left(\frac{2\pi}{365} \cdot (doy - 81)\right), \tag{7}$$

where $d_{s,mlt6}$ and $d_{s,mlt12}$ are the maximum and minimum melt factors on 21 June and 21 December, respectively, and *doy* is the day of the year (Fontaine et al., 2002).

Snow sublimation in the snowmelt process is considered to occur only for fresh snow. To take into account snow sublimation, fresh snow is multiplied by a factor, namely:

$$Factor_t = 1 - \frac{\log(SWE_t + 1)}{\log(SFSWE)}, \tag{8}$$

(see Table 1 for the definition of SFSWE). Calculations with Eqs. (1) through (8) are carried out at the grid-cell scale, at a 1 km × 1 km resolution.

3.1.2. Snowmelt simulation using snow cover area as a reference

For the snowmelt simulation using SCA as the calibration reference, equations for calculating SWE and snowmelt are the same as those for the snowmelt calibrated with SWE [Eqs. (3)–(7)]. However, the simulated SWE must be converted to SCA using the Swe2ScaTh parameter (see Table 1), in order to make use of the satellite-based estimate of SCA, i.e., if SWE in a grid cell exceeds Swe2ScaTh, then this grid cell is considered to be covered by snow:

$$SCA = \begin{cases} 1 & SWE \geq Swe2ScaTh \\ 0 & SWE < Swe2ScaTh \end{cases}, \tag{9}$$

Then, by comparing simulated and remotely-sensed SCA, a set of suitable temperature thresholds for snowmelt can be derived. Note that the calibration references (i.e., remotely sensed SWE or SCA) were only employed in the calibration period to derive the parameters for simulated snowmelt: they were not used as forcing data in the snowmelt

module. Meanwhile, snow sublimation in this case differs from that in Section 3.1.1, and is calculated from

$$SWE_{t+1} = (SWE_t - SM_t + P_{s,t}) \cdot SFSCA, \tag{10}$$

where SFSCA is used to describe the percentage of snow remaining after sublimation.

3.1.3. Glacier melt simulation

The glacier melt module employed in this study is based on the temperature-index method and degree-day factor. Similar to the remotely sensed SWE or SCA, parameters of the glacier melt module (e.g., the glacier melt temperature and degree-day factor) must be calibrated against some reference for glacier ablation. Unlike remotely sensed SWE or SCA, glacier ablation at the regional scale is difficult to measure directly. Therefore, this is inferred using the mass balance approach, i.e., the glacier mass depletion is equal to the GRACE-derived TWS change minus modelled soil moisture and SWE changes. The glacier melt module was subsequently coupled to CREST, and the proportional contribution of glacier meltwater to total runoff can therefore be quantified (Chen et al., 2017b).

Note that the glacierized area of the HRYR is highly localized (Fig. 1), and the glacier mass change is not a dominant component in the regional change in TWS, which exhibits an increasing trend, mostly owing to increased precipitation (Jiang et al., 2007; Long et al., 2017; Yang et al., 2004). However, the glacier mass for the headwater region has been decreasing based on in situ measurements over recent decades (Chao et al., 2017; Kang et al., 2015). In addition, the signal-to-noise ratio (SNR) of the GRACE signal over the HRYR is relatively low (Long et al., 2017). Therefore, calibrating the parameters associated with the glacier module using the GRACE-derived TWS change is no longer suitable for this study area (Chen et al., 2017b). Here, we applied CREST-snow to a surrounding basin, i.e., the Lancang River basin (the Upper Mekong River), where the GRACE-derived TWS change exhibits a consistent decreasing trend in line with glacier mass depletion elsewhere. The glacier melt parameters for the Lancang River basin were subsequently transferred to the HRYR (i.e., melting temperature threshold of -0.7 °C and degree-day factor of 7.09 mm °C^{-1}d^{-1} for ice melt). We also demonstrated the reasoning behind the parameter transferability, as described in Section 3 of the Supporting Information.

3.2. Model performance metrics

To evaluate the performance of the modeling results, three statistical metrics were considered, i.e., the Nash-Sutcliffe efficiency coefficient (*NSE;* Nash and Sutcliffe, 1970), mean relative bias (*Bias*), and Pearson correlation coefficient (*CC*). The objective function of the modeling is calculated as follows:

$$Obj = \frac{(NSE + 1 - |Bias| + CC)}{3}, \tag{11}$$

In the case of calibration using the SWE reference, each metric was computed between the simulated SWE and the PMW SWE. During the calibration, Obj_{SWE} should approach 1 in deriving the best modeling

results. In the case that SCA was the calibration reference, the same metrics (i.e., Obj_{SCA}, NSE_{SCA}, $Bias_{SCA}$, and CC_{SCA}) were calculated between the simulated and MODIS-based SCA.

3.3. Evaluation of snowmelt based on hydrological consistency

It is challenging to evaluate snowmelt directly, which is a component of total runoff, and is difficult to observe and disaggregate. Evaluating melting processes with a single dataset, such as SCA or SWE is also unreliable. Hydrological consistency was proposed to seek improvements of evaluating hydrological simulation (McCabe et al., 2008). Evaluation based on hydrological consistency (EHC) implies that model outputs can be evaluated using different sources of information for model calibration according to the consistency among model variables. Taking snowmelt evaluation as an example, assuming that the snowmelt module accurately depicts the snowmelt process, different sources of information for snow (e.g., SWE or SCA) may result in significant differences in snowmelt simulations. We can evaluate the reliability of modelled snowmelt by comparing it with different calibration references. If modelled snowmelt from different calibration references exhibits high consistency, the proportional contribution of the snowmelt to total runoff should be close and regarded as reliable. Therefore, the EHC for snowmelt simulation is measured by the ratio of snowmelt runoff contributions to total runoff with either SWE or SCA as the calibration reference (R_c; Eq. (12)), and the simulated snow meltwater is more reliable when R_c is closer to 1:

$$R_c = \frac{C\text{swe}}{C\text{sca}}, \tag{12}$$

where C_{swe} and C_{sca} are the snowmelt runoff contributions to total runoff with either SWE or SCA as the calibration reference.

The framework of simulating and evaluating snow and glacier melt processes is illustrated in Fig. 3. In summary, first, we simulated SWE and SCA using CREST-snow with the selected precipitation product and land surface and air temperatures as input forcing variables. Either remotely sensed SWE or SCA (after resampling) was employed as the reference in the calibration of model parameters (Table 1 in Section 3.1.1), and the simulated snowmelt runoff was compared and validated based on the EHC. Second, glacier meltwater was simulated using the glacier melt module with the parameters transferred from the Lancang River basin (referring to Section 3.2). Third, the simulated snowmelt under the SWE and SCA scenarios in step I was combined with the selected precipitation product and the simulated glacier meltwater in step II to generate total runoff. Fourth, proportional contributions of the snow and glacier meltwater to total basin discharge were determined.

4. Results

4.1. Time series of simulated SWE and SCA

Fig. 4 illustrates the simulated daily SWE (Fig. 4(a)–(c)) and SCA (Fig. 4(d)–(f)) time series over 2003–2014, during which the warm-up period was from January 2003 to June 2003, the calibration period spanned three and a half years from July 2003 to December 2006, and the validation period spanned eight years from January 2007 to December 2014. Table 2 presents the details for all metrics.

For the SWE simulations (Fig. 4(a)–(c)), the simulated and remotely sensed SWE are generally consistent, with NSE and CC values of up to 0.56 and 0.75, respectively, during the calibration period, and NSE and CC values of 0.47 and 0.71, during the validation period. In addition, the snowmelt module could catch the onset and end of SWE. Furthermore, the resolution of the model output is considerably higher (i.e., at 1 km) than that of the PMW remote sensing data (~27 km × 27 km). Apart from the overall consistency, the simulated SWE was generally underestimated, and exhibited disparities with the remotely sensed SWE at the beginning of the snow accumulation season. According to

published studies, PMW retrievals tend to overestimate snow-covered areas over the Tibetan Plateau, which may result in the discrepancy between the simulated SWE and PMW SWE (Dai et al., 2017; Dai et al., 2018; Savoie et al., 2009).

For the SCA simulation (Fig. 4(d)–(f)), the snowmelt module performed well during the calibration period, with an NSE of 0.60 and CC of 0.83, but the performance degraded during the validation period, with an NSE of 0.39 and CC of 0.71. Overall, the simulated SCA was generally consistent with the eight-day maximum SCA extent from MODIS, whereas an underestimation for some days was observed, reflected by a negative bias in both the calibration and validation periods. Unlike the within-year single peak captured by PMW SWE, the eight-day maximum SCA extent exhibited multiple peaks during the snow accumulation season, and this characteristic is also shown in the simulated SCA. Published studies indicate that the snow cover over the TP changes rapidly, and it is generally shallow, resulting in multiple peaks in SCA within a single year (Li et al., 2014; Zhang et al., 2014; G. Zhang et al., 2012).

In comparing SWE and SCA simulations, it can be found that the SCA simulation appeared to be slightly better than that of the SWE simulation during the calibration period, in terms of both NSE (0.6 for SCA and 0.56 for SWE) and CC (0.83 for SCA and 0.76 for SWE). However, the overall performance of the SWE simulation was better during the validation period, and increased by ~11% in terms of the NSE for the entire period (0.44 for SCA and 0.49 for SWE). Given that SWE and SCA simulations were performed at different timescales, monthly averages were computed to reduce the impact of the difference in timescale and high-frequency noise for daily and eight-day simulations (Fig. 5 and Table 3). It was found that the SWE simulation was generally better than the SCA simulation, with the NSE for the SCA simulation increasing by ~28% for the validation period relative to that of the eight-day timescale (an NSE of 0.39 at the eight-day timescale and 0.50 at the monthly timescale). In general, the performance of both the SWE and SCA simulations at the monthly scale increased markedly in both the calibration and validation periods compared with those at the daily and eight-day timescales, exhibiting an improved consistency on a longer timescale due to reduction of noise at shorter timescales.

4.2. Spatial distribution of simulated SWE and SCA

Fig. 6 illustrates the spatial distribution of the mean seasonal (fall and winter) and annual simulated and PMW-based SWE values for the 2003–2014 period, indicating a general consistency between the simulations and the remotely sensed retrievals across space and in magnitude. Moreover, the simulated and remotely sensed SWE values in winter are generally larger than those in the fall and for the entire year. SWE is mainly distributed at the fringe of the HRYR, particularly over the southwest and southeast areas (the left panel in Fig. 6). The simulated SWE is generally underestimated, which may result from uncertainty in PMW SWE, particularly in the southeast, where the remotely sensed SWE is above 2 mm in all three cases but the simulated SWE is close to zero.

With the same forcing in the SWE simulation, except with the calibration reference replaced by remotely sensed SCA from MODIS, Fig. 7 illustrates the spatial distribution of the mean seasonal (fall and winter) and annual simulated and remotely sensed SCA values from MODIS for the 2003–2014 period, revealing a higher consistency between the simulated and remotely sensed SCA than for the simulations based on SWE. Similar to the SWE distribution in Fig. 6, higher SCA values are distributed along the fringe of the HRYR and around the high-elevation mountains within it (the left panel of Fig. 7). The SCA simulation is highly consistent with the remotely sensed SCA in terms of the spatial distribution. Moreover, unlike the comparison for SWE (Fig. 6), SCA's in the southeast are more highly consistent (Fig. 7). Therefore, using the remotely sensed SCA to calibrate the snowmelt module may be still effective, although uncertainty is present owing to
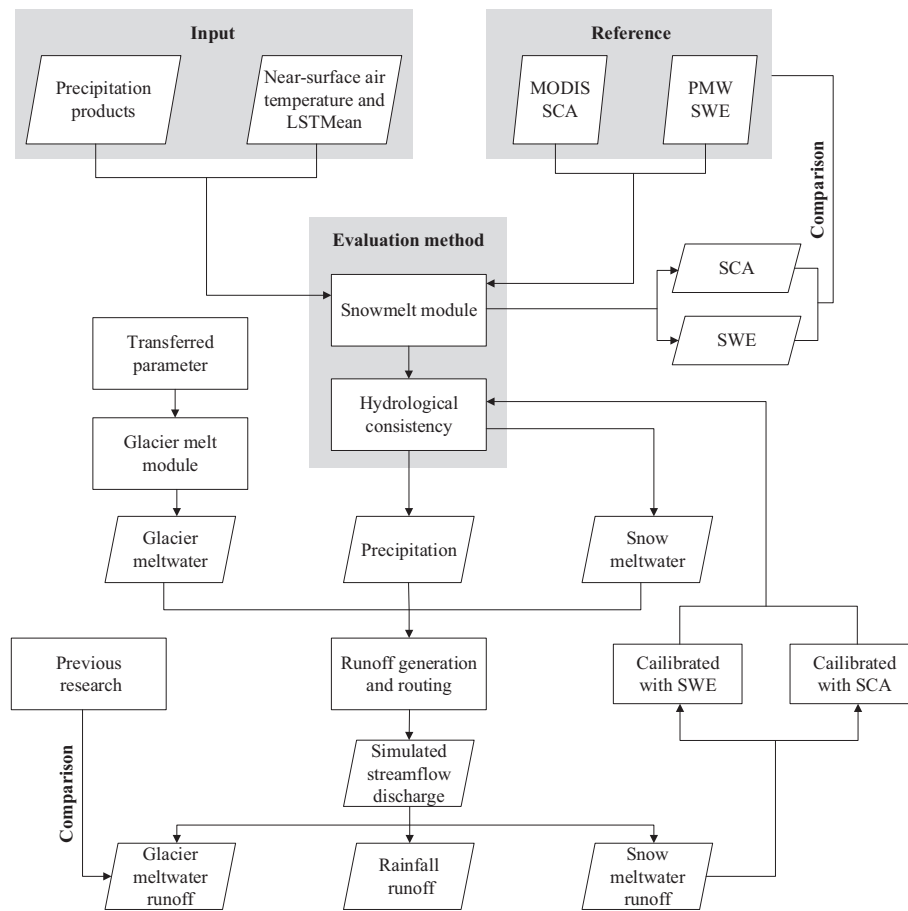
Fig. 3. Framework of simulating and evaluating the snow and glacier melt processes. CREST-snow was employed for the hydrological simulation with various precipitation products and air and land surface temperatures as input variables. PMW SWE and MODIS SCA were employed as references for model calibration.

potential cloud contamination.

In addition, by comparing the spatial distributions of MODIS SCA (Fig. 7) and PMW SWE (Fig. 6), a discrepancy is observed, in particular across the east of the HRYR. The PMW SWE with a relatively coarse spatial resolution of ~27 km × 27 km exhibits a more extensive distribution than the MODIS SCA with a higher spatial resolution of ~500 m × 500 m, particularly in the east and southeast areas of the headwater region. Considering the uncertainty and coarse spatial resolution of the PMW SWE, the spatial distribution of the MODIS SCA appears to be more reliable (Dai et al., 2017; Foster et al., 2005). This indicates the necessity of developing SWE products of higher spatial resolution by incorporating multisource remote sensing data of comparable resolution, such as optical SCA, thermal infrared LST, and PMW brightness temperatures. For example, Xiao et al. (2018) developed a snow-depth retrieval algorithm, which is effective in retrieving snow depth at various scales using support vector regression. Similar work will be required to improve the reliability and spatial resolution of remotely sensed SWE, and consequently the consistency between simulated and remotely sensed SWE.

4.3. Simulation of meltwater and total runoff

By applying the parameters associated with the snowmelt process calibrated using either SWE or SCA, time series representing the snowmelt runoff were derived using CREST-snow, reflecting an overall high consistency for the two scenarios (Fig. 8). Compared with the time series calibrated using SCA, the onset of snowmelt calibrated with SWE occurs sooner, resulting mainly from discrepancy in snow sublimation in the SCA and SWE calibration scenarios, as well as the snowmelt

parameters. We summed the total amounts of snowfall, snow sublimation, and snowmelt over 2003–2014 for the two scenarios (Table 4). The total snowfall under the SCA calibration scenario (597 mm) is significantly higher than that under the SWE calibration scenario (458 mm). However, the snowmelt under the SCA calibration scenario (225 mm) is slightly lower than that under the SWE calibration scenario (258 mm), owing to the higher snow sublimation. In fact, snow sublimation has a clear effect on the TP, and more than 50% of snow-mass loss is caused by this process (Qin et al., 2006). Therefore, large snow-sublimation levels captured by the simulation seem justified.

The MODIS SCA fluctuates more frequently in winter (Figs. 4–5), indicating greater snow sublimation. Only with larger snow sublimation can the amount of snow increase or decrease rapidly within a short time period. The larger snow sublimation under the SCA calibration scenario also corresponds to more snowfall, resulting in a similar magnitude of snowmelt under the two scenarios (SCA scenario: 225 mm, SWE scenario: 258 mm).

In addition to temperature changes, other radiative and aerodynamic variables that affect snow sublimation and snow accumulation also exhibit significant trends, e.g., net radiation, wind speed, and relative humidity. McVicar et al. (2012) found that the wind speed over the TP exhibited a large decreasing trend, by reviewing 148 regional studies. Solar radiation was not globally stable over a period of years, exhibiting a widespread decrease from 1950 to 1980 and a partial recovery in many locations over recent years (Wild, 2009). Water vapor, or atmospheric humidity, is a key component driving atmospheric processes, and hence it is fundamental for hydrological studies. Willett et al. (2008) concluded that surface humidity increased significantly worldwide from 1973 to 2003, thus greatly impacting atmospheric
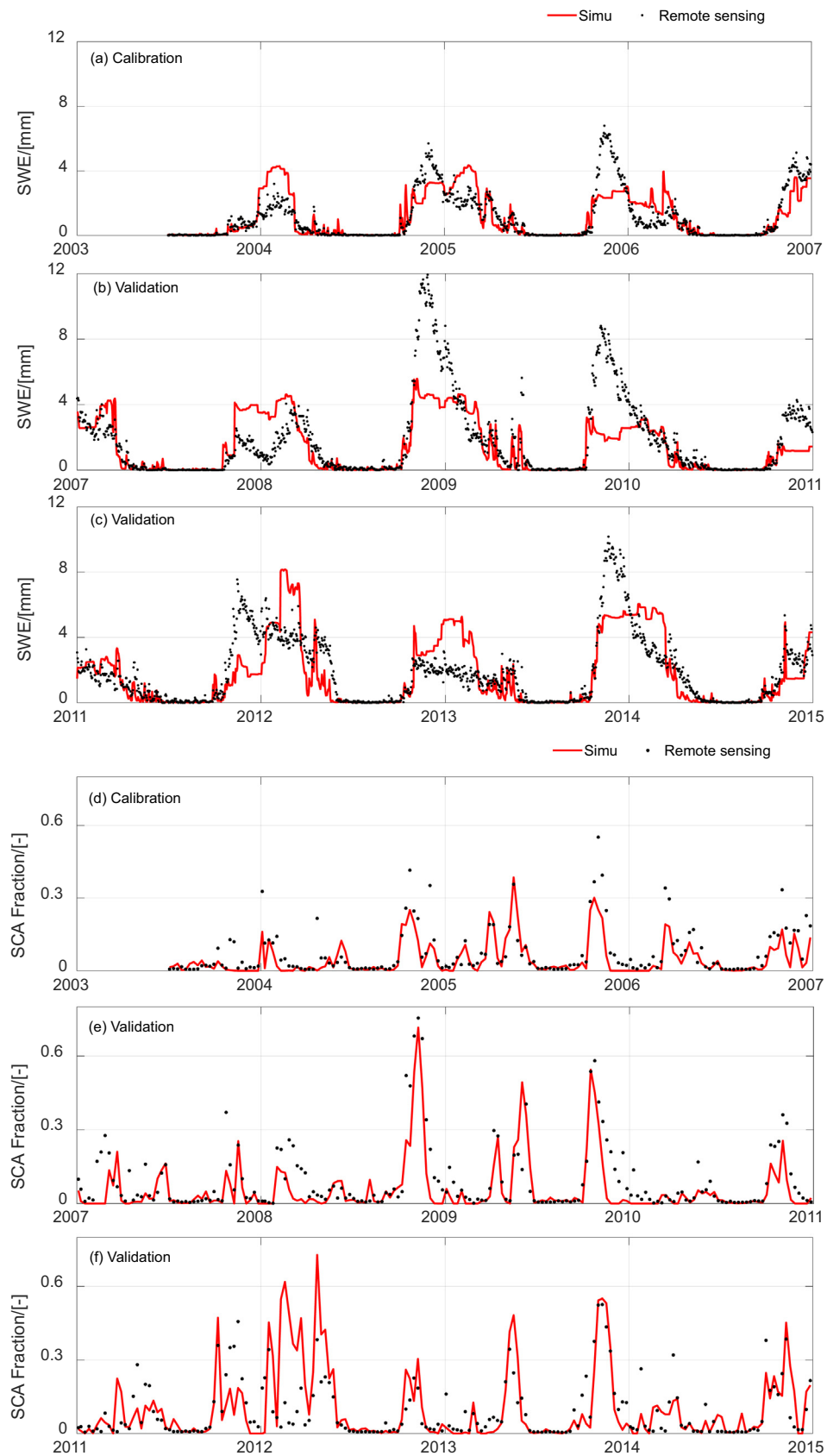
Fig. 4. Time series of remotely sensed and simulated SWE (daily, (a)–(c)) and SCA (eight-day, (d)–(f)) from the snowmelt module forced for the July 2003–December 2014 period.

Table 2
Performance metrics for daily SWE and SCA simulations in the calibration period (July 2003–December 2006), validation period (January 2007–December 2014), and the entire study period (July 2003– December 2014).

Period	SWE				SCA			
	Obj (−)	NSE (−)	CC (−)	Bias (%)	Obj (−)	NSE (−)	CC (−)	Bias (%)
Calibration (Jul 2003–Dec 2006)	0.76	0.56	0.76	3.24	0.78	0.60	0.83	−9.21
Validation (Jan 2007–Dec 2014)	0.72	0.47	0.71	−2.57	0.67	0.39	0.71	−7.78
Entire period	0.74	0.49	0.73	0.97	0.70	0.44	0.73	−8.74

Table 3
Performance metrics for the monthly SWE and SCA simulations in the calibration period (July 2003–December 2006) and validation period (January 2007–December 2014).

Period	SWE			SCA		
	NSE (−)	CC (−)	Bias (%)	NSE (−)	CC (−)	Bias (%)
Calibration (Jul 2003–Dec 2006)	0.61	0.79	4.69	0.60	0.86	−15.42
Validation (Jan 2007–Dec 2014)	0.54	0.75	−3.63	0.50	0.76	−9.18
Entire period	0.55	0.76	1.40	0.52	0.77	−11.81

processes. Among these variables, temperature is the only variable considered in this study, and further research related to other variables will be required to better simulate snow and glacier sublimation in the future.

Peaks of snowmelt runoff normally occur during spring for both cases, but there are multiple peaks for some years, with the second peak in fall. This is a combined effect of precipitation and temperature. Typically, the snowfall may exhibit peaks during fall, when the temperature may still be high, resulting in the generation of snowmelt runoff. Furthermore, the contributions of snowmelt to the total basin discharge are 6.7 and 6.5% for the SWE and SCA scenarios, respectively, yielding an R_c-value of 1.03. The high consistency of the contributions from these two scenarios demonstrates the overall reliability of the calculations, indicating that snowmelt is an important source (~7%) of runoff in the HRYR, particularly in spring.

The glacier melt runoff generally exhibits small fluctuations during the study period, and is significantly smoother than snowmelt runoff in the annual cycle (Fig. 9). The reason for this is that glacier melt runoff is more sensitive to changes in temperature than precipitation, whereas snowmelt runoff is largely affected by precipitation along with temperature (Singh and Kumar, 1997). Temperature typically exhibits regular changes in the annual cycle, whereas precipitation is considerably more random, leading to fluctuations in snowmelt runoff. In addition, the occurrences of peaks in glacier melt runoff are typically later than the total runoff. The reason for this is that the total runoff is dominated by rainfall runoff, which reaches peaks in July or August, and the glacier melt runoff reaches peaks in August or September. The contribution of the glacier meltwater to the total basin discharge was estimated to be 5.2%, which is comparable with the snowmelt contributions.

The total runoff simulation from CREST-snow was shown in Fig. 9 and Table 5. The simulated discharge at the Zhimenda gauging station is greatly consistent with the daily discharge observations, with an *NSE* of up to 0.87 and 0.80 during the calibration and validation periods. However, the simulation shows a slight overestimation of streamflow

peaks with a positive *Bias*, mainly in the later period. During the low flow period, such as in early spring, the snowmelt exhibits peaks (Fig. 8) and is the main source of streamflow. Overall, CREST-snow performs well in both high and low flow periods, implying the potential for future runoff predictions.

The contributions of snow and glacier meltwater to total basin discharge during the different months and seasons are presented (Fig. 10 and Table 6). The monthly climatology of glacier meltwater is similar to the total runoff, peaking in August (Fig. 10). Nevertheless, the monthly climatology of snowmelt varies considerably with glacier meltwater. Snow in the headwater region begins melting in spring, peaks, and then decreases, reaching a second peak in the fall, as explained above. Snowmelt accounts for 33% of the total basin discharge in spring (MAM), representing a critically important source of runoff.

Although the snowmelt attains a second peak during the fall (SON), its contribution to the total basin discharge is relatively low during this period, because the magnitude of the basin discharge is large. In addition, snowmelt runoff still exists in summer because of melting of the remaining snowpack. Snowmelt runoff decreases to its lowest value in early autumn and increases to form a second peak in fall. For glacier meltwater, the percent contributions appear to be similar across all seasons except spring, and are smaller than snowmelt, indicating that snowmelt is a more important component of the total runoff in the HRYR, particularly during spring and winter.

5. Discussion

In the present work, we have evaluated simulated snowmelt based on the EHC. The contributions of snow and glacier meltwater to the total basin discharge have been quantified. This study provides an effective and practical approach to validate the accuracy of snowmelt runoff simulations over poorly gauged and ungauged river basins. The results of the study are encouraging, but some questions remain and further work is needed.

5.1. Sensitivity analysis and validation of snowmelt parameters

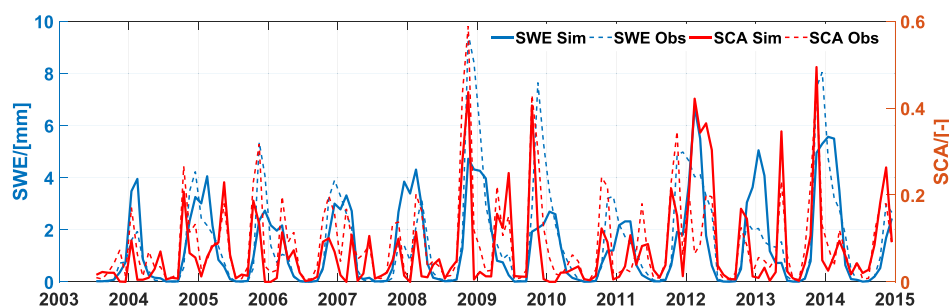For snowmelt modeling, effects of temperature thresholds (i.e.,

Fig. 5. Monthly time series of remotely sensed and simulated SWE and SCA from the snowmelt module for the 2003–2014 period.
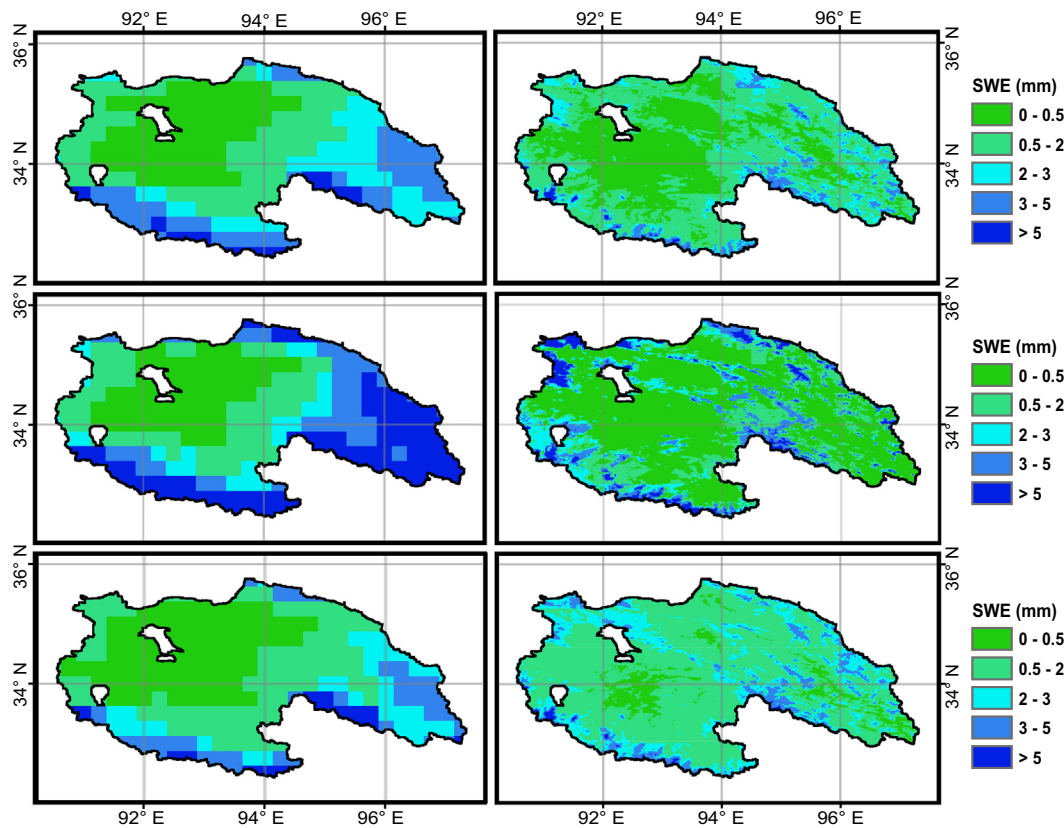
Fig. 6. Spatial distributions of PMW SWE (left panel) and simulated SWE (right panel) for fall (top panel) and winter (middle panel), and the mean annual SWE (bottom panel) for the period 2003–2014.

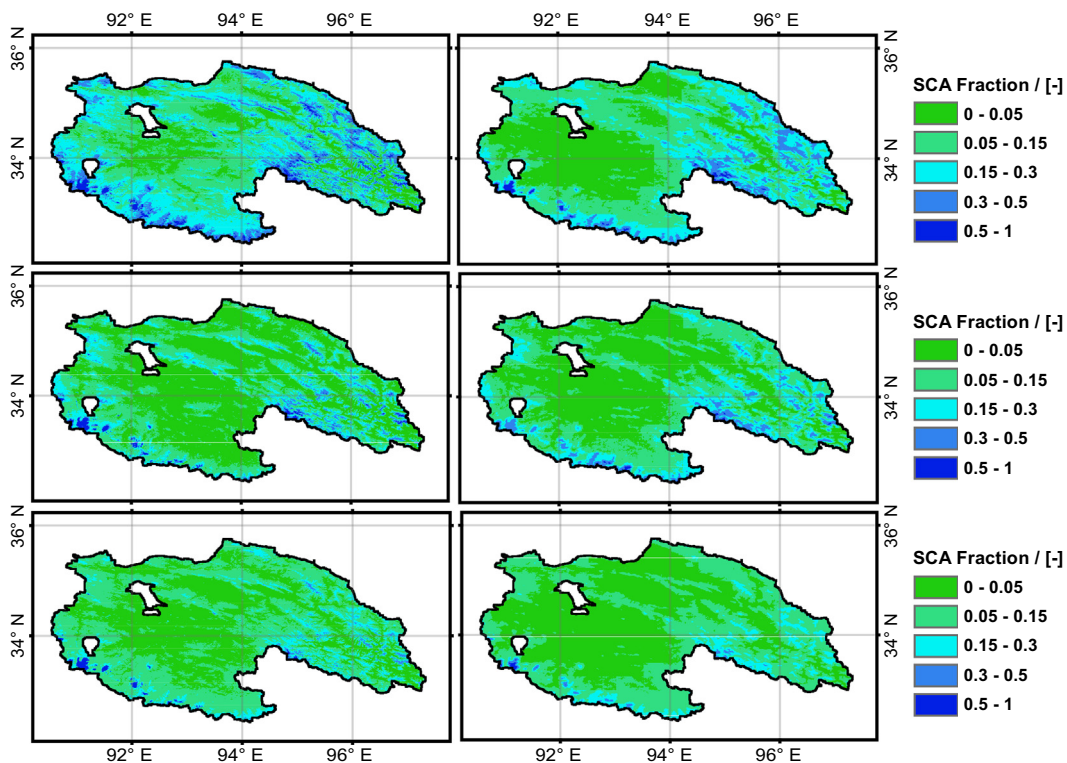**Fig. 7.** Spatial distribution of the remotely sensed SCA from MODIS (left panel) and the simulated SCA (right panel) for fall (top panel) and winter (middle panel), and the mean annual SCA (bottom panel) for the 2003–2014 period.
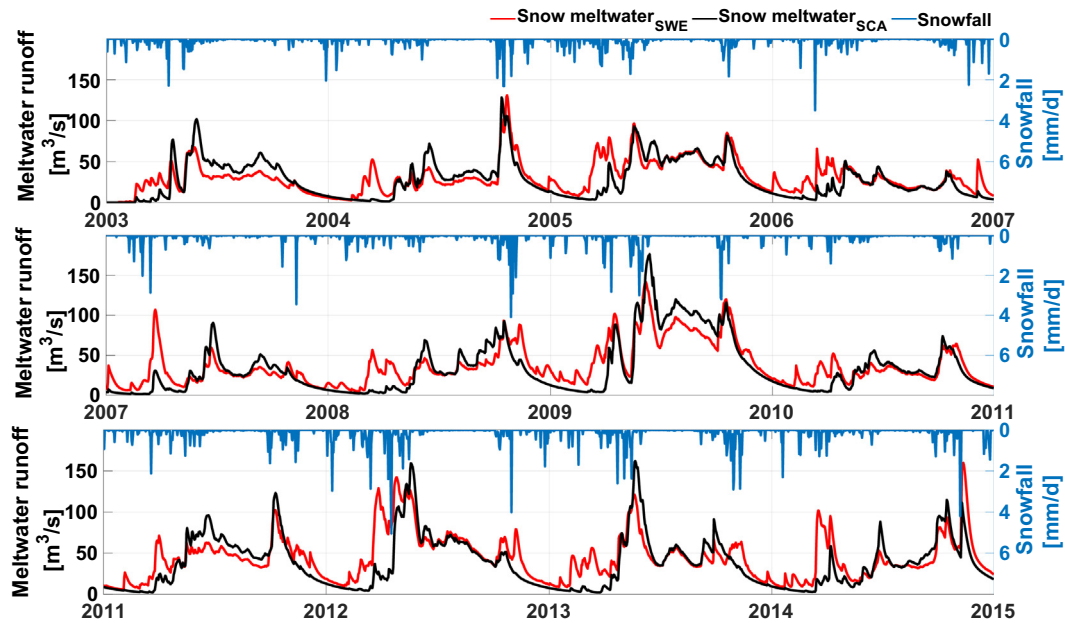
Fig. 8. Snowmelt runoff time series calibrated using PMW SWE (red line) and MODIS SCA (black line), and snowfall time series (SWE calibration) for the 2003–2014 period. (For interpretation of the references to colour in this figure legend, the reader is referred to the web version of this article.)

Table 4
Total amounts of snowfall, snow sublimation, and snowmelt in the SCA and SWE calibration scenarios during 2003–2014.

Scenario	Snowfall (mm)	Snow sublimation (mm)	Snowmelt (mm)
SCA	597	393	225
SWE	458	205	258

Table 5
Performance metrics for total runoff simulation in the calibration (Jul 2003–Dec 2006) and validation periods (January 2007–December 2014).

Period	NSE_Q (−)	NSE_{LogQ} (−)	CC (−)	Bias (−)
Calibration (Jul 2003–Dec 2006)	0.87	0.77	0.93	0.07
Validation (Jan 2007–Dec 2014)	0.80	0.76	0.91	0.12
Entire period	0.82	0.77	0.92	0.11

$T_{s,mlt}$, T_s, and T_r) and degree-day factors (i.e., $d_{s,mlt6}$ and $d_{s,mlt12}$) are significant. To figure out the critical parameters in snowmelt simulation, we performed a sensitivity analysis of these parameters. Parameters were classified into three groups: (1) T_s, and T_r which determine precipitation phases; (2) $T_{s,mlt}$ which determines snowmelt

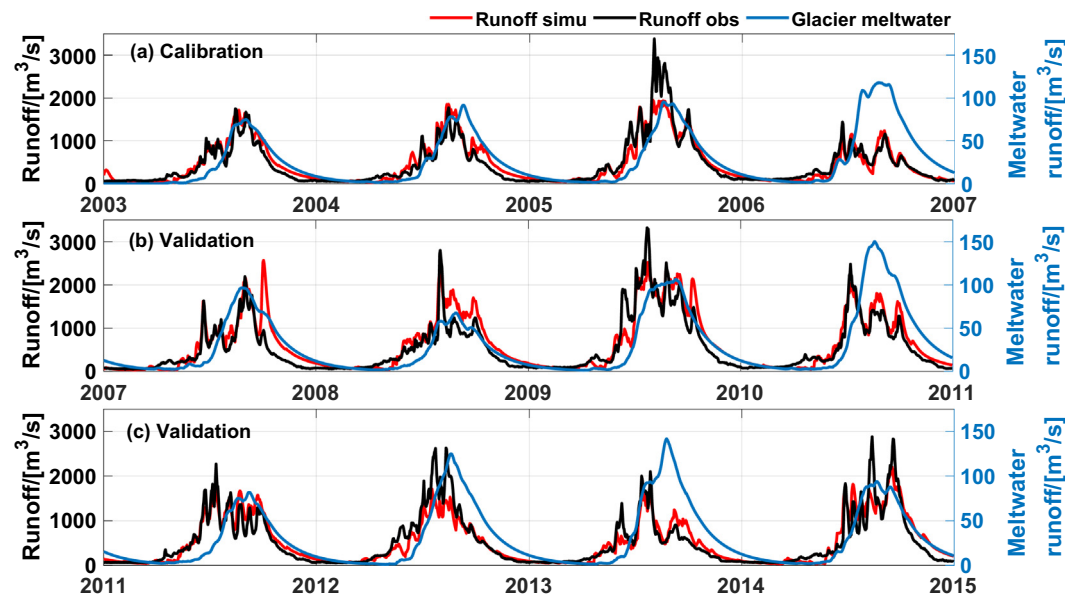**Fig. 9.** Time series for total runoff simulation (red line), observations (black line), and glacier melt runoff (blue line) during 2003–2014, with the warm-up period from January 2003–June 2003, the calibration period from July 2003–December 2006, and the validation period from January 2007–December 2014. (For interpretation of the references to colour in this figure legend, the reader is referred to the web version of this article.)
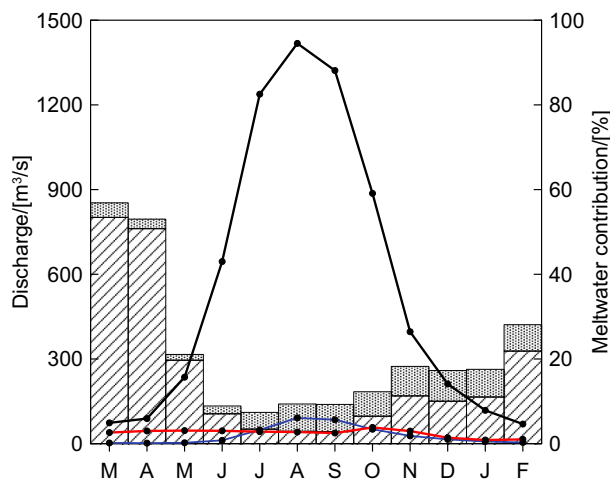
Fig. 10. Mean monthly total basin discharge (black line, left axis), and snow and glacier meltwater discharge (red and blue lines, respectively, left axis). The histograms show contributions of snow (slash bars, right axis) and glacier (dotted bars, right axis) meltwater to the total runoff. (For interpretation of the references to colour in this figure legend, the reader is referred to the web version of this article.)

Table 6
Contributions of snow and glacier meltwater to the total basin discharge in different seasons based on the mean monthly total snow and glacier meltwater runoff and total runoff (spring spans MAM, summer spans JJA, autumn spans SON, and winter spans DJF in the following year).

Type	Spring	Summer	Autumn	Winter
Snowmelt	32.9%	3.9%	5.4%	12.4%
Glacier melt	2.0%	4.6%	6.3%	6.9%

Table 7
Experiments with a changed snowfall and rainfall temperature threshold (T_s and T_r). Highlighted parameters and results are referred to as the baseline SWE scenario for model calibration.

No.	T_r [°C]	T_s [°C]	Mean annual snowmelt runoff depth [mm]	Mean annual runoff depth [mm]	Contribution [%]	NSE [−]	Bias [−]	CC [−]
1	47.9	46.5	116	123.6	93.89	0.84	0.07	0.92
2	3.9	2.5	44	126.3	34.82	0.83	0.10	0.92
3	1.9	0.5	26.6	126.4	21.08	0.83	0.10	0.92
4	−0.1	−1.5	15.2	126.6	12	0.83	0.10	0.92
5	**−2.1**	**−3.5**	**8.5**	**127.5**	**6.69**	**0.82**	**0.11**	**0.92**
6	−4.1	−5.5	5.1	129.1	3.97	0.81	0.12	0.92
7	−6.1	−7.5	3.3	130.5	2.56	0.81	0.13	0.91
8	−8.1	−9.5	2.3	131.7	1.78	0.81	0.14	0.91
9	−10.1	−11.5	1.7	132.8	1.26	0.80	0.15	0.91
10	−52.1	−53.5	0	135.9	0	0.79	0.18	0.91

temperature; and (3) $d_{s,mlt6}$ and $d_{s,mlt12}$ which determine snowmelt rates. Each group had ten experiments with a specific change in the parameters, and then we compared the contributions of snowmelt runoff to total runoff for different parameters. For group (1) and (2), we increased or decreased T_s, T_r and $T_{s,mlt}$ by 2 °C, 4 °C, 6 °C, 8 °C, and 50 °C for each experiment. For group (3), we increased or decreased $d_{s,mlt6}$ and $d_{s,mlt12}$ by 0.5 mm °C^{-1} d^{-1}, 1.0 mm °C^{-1} d^{-1}, 1.5 mm °C^{-1} d^{-1} and 2.0 mm °C^{-1} d^{-1} for each experiment. Results shown in Tables 7–9 indicate that the snowfall temperature threshold is the most sensitive parameter for snowmelt simulation, and an increase of 2 °C in T_s would result in an increase of the contribution of snowmelt runoff to total

Table 8
Experiments with a changed snowmelt temperature threshold ($T_{s,mlt}$). Highlighted parameters and results are referred to as the baseline SWE scenario for model calibration.

No.	$T_{s,mlt}$ [°C]	Mean annual snowmelt runoff depth [mm]	Mean annual runoff depth [mm]	Contribution [%]	NSE [−]	Bias [−]	CC [−]
11	45.4	0	110.9	0	0.83	−0.04	0.91
12	3.4	3.4	118.2	2.91	0.84	0.03	0.92
13	1.4	4.1	121.3	3.42	0.83	0.05	0.92
14	−0.6	5.2	123.6	4.21	0.83	0.07	0.92
15	−2.6	6.6	125.3	5.29	0.83	0.09	0.92
16	**−4.6**	**8.5**	**127.5**	**6.69**	**0.82**	**0.11**	**0.92**
17	−6.6	10.9	130.2	8.36	0.81	0.13	0.92
18	−8.6	12.8	132.3	9.68	0.81	0.15	0.91
19	−10.6	14.1	133.8	10.55	0.80	0.16	0.91
20	−54.6	16.3	136.3	11.99	0.79	0.18	0.91

runoff by a factor of ~1.7. The sensitivity of the model to the snowmelt temperature threshold is much smaller; a decrease of 2 °C in $T_{s,mlt}$ would result in an increase of the snowmelt runoff contribution by a factor of ~1.2. Compared to T_s and $T_{s,mlt}$, degree-day factors are the least sensitive parameters.

By using either remotely sensed SCA or SWE for model calibration, we have derived the parameters for snowmelt simulation. The results indicate that the snowfall temperature thresholds for both calibration references are very close, i.e., −3.5 °C for the SCA calibration scenario and −4.0 °C for the SWE calibration scenario. According to the study by Ding et al. (2014), our snowfall temperature thresholds are within a reasonable range. This is an important finding because use of different remote sensing sources for model calibration can derive consistent parameters, which are critical to snowmelt simulation.

In order to further validate the reliability of the derived snowmelt model parameters, snowfall from our model was compared with limited in situ snowfall measurements (Fig. 11). Table 10 shows annual cumulative snowfall and Table 11 lists statistical metrics used in the comparison. Note that the probability of detection (POD), false alarm ratio (FAR), and the critical success index (CSI) are used to describe the contingency of the simulated snowfall here. The POD gives the fraction of snowfall events that the simulation detects among all the actual snowfall events, FAR gives the fraction of unreal events among all the events the simulation detects, and CSI gives the overall fraction of correctly reflected snowfall events by simulation, which can be expressed as a function of POD and FAR (Ebert et al., 2007; Tang et al., 2016; Tang et al., 2018a).

The consistency between snowfall simulation and observation is generally acceptable in terms of both timing and magnitude, with CC of 0.55, Bias of 0.55%, POD of 0.65, FAR of 0.47, and CSI of 0.41. Bias values from Rasmussen et al. (2011) and Ikeda et al. (2010) are higher than 10%, and CC from Dudhia et al. (2008) is about 0.52, indicating that the simulated snowfall here is comparable with previous studies, given that our study region is in a poorly gauged area. The generally high consistency between the snowfall simulation and observation indicates the reliability of the derived parameters, particularly for the snowfall temperature threshold that is the most sensitive parameter in snowmelt simulation.

5.2. Simulation of meltwater

Comparisons between our study and previous studies are shown in Table 12. Zhang et al. (2013) used the Variable Infiltration Capacity (VIC) land surface hydrology model with a degree-day glacier-melt scheme (VIC-glacier model) to simulate snow and glacier melt processes in the headwaters of the Yangtze River. They found that the

Table 9
Experiments with a changed degree-day factor. Highlighted parameters and results are referred to as the baseline SWE scenario for model calibration.

No.	$d_{s,mlt6}$ [mm °C^{-1} d^{-1}]	$d_{s,mlt12}$ [mm °C^{-1} d^{-1}]	Mean annual snowmelt runoff depth [mm]	Mean annual runoff depth [mm]	Contribution [%]	NSE [−]	Bias [−]	CC [−]
21	12	7.5	8.7	127.7	6.79	0.79	0.18	0.91
22	11.5	7	8.6	127.6	6.77	0.82	0.11	0.92
23	11	6.5	8.6	127.6	6.74	0.82	0.11	0.92
24	10.5	6	8.6	127.5	6.71	0.82	0.11	0.92
__25__	__10.2__	__5.7__	__8.5__	__127.5__	__6.69__	__0.82__	__0.11__	__0.92__
26	9.5	5	8.5	127.4	6.64	0.82	0.11	0.92
27	9	4.5	8.4	127.4	6.60	0.82	0.11	0.92
28	8.5	4	8.3	127.3	6.55	0.82	0.10	0.92
29	8	3.5	8.3	127.2	6.49	0.82	0.10	0.92
30	7.5	3	8.2	127.1	6.42	0.82	0.10	0.92
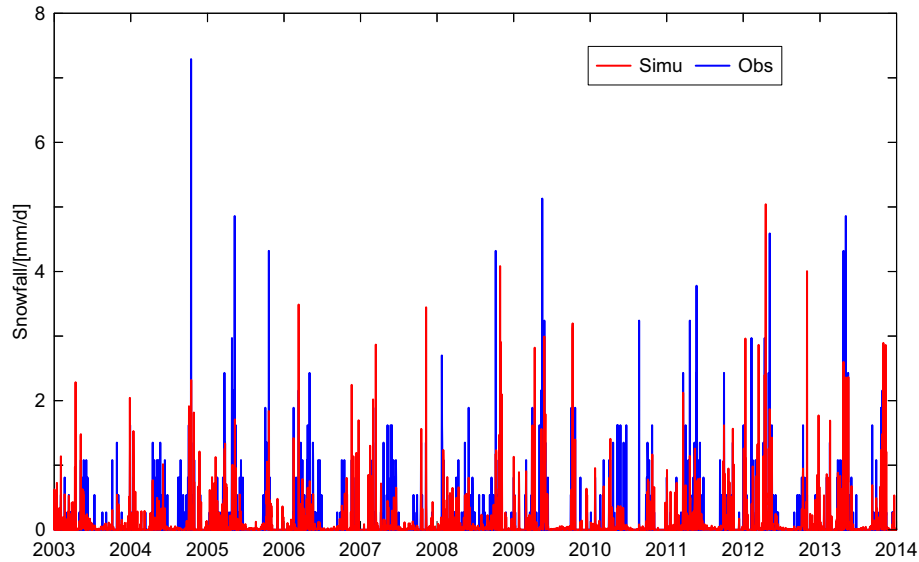
Fig. 11. Time series of snowfall from the model simulations and gauge-based mean observations at the basin scale during January 2003–December 2013.

Table 10
Annual cumulative snowfall (mm/yr) from model simulations and gauge-based mean observations at the basin scale during January 2003–December 2013.

Year	2003	2004	2005	2006	2007	2008	2009	2010	2011	2012	2013
Simulated	29.1	31.5	38.4	30.7	27.5	38.8	46.6	21.0	35.4	61.9	50.3
Observed	21.6	37.3	52.9	36.5	28.4	40.5	46.4	32.9	40.8	57.0	47.5

Table 11
Statistical metrics used in evaluating the simulated snowfall against gauge-based observations[a].

Statistic metrics	Equation	Perfect value	Value
Correlation coefficient (CC)	$CC = \dfrac{\frac{1}{N}\sum_{n=1}^{N}(S_n - \bar{S})(G_n - \bar{G})}{\sigma_S \sigma_G}$	1	0.55
Relative bias (Bias)	$Bias = \dfrac{\sum_{n=1}^{N}(S_n - G_n)}{\sum_{n=1}^{N} G_n}$	0	0.55%
Root mean squared error (RMSE)	$RMSE = \sqrt{\frac{1}{N}\sum_{n=1}^{N}(S_n - G_n)^2}$	0	0.33 mm/d
Probability of Detection (POD)	$POD = \dfrac{n_{11}}{n_{11} + n_{01}}$	1	0.65
False Alarm Ratio (FAR)	$FAR = \dfrac{n_{10}}{n_{11} + n_{10}}$	0	0.47
Critical Success Index (CSI)	$CSI = \dfrac{n_{11}}{n_{11} + n_{01} + n_{10}} = \dfrac{1}{\frac{1}{1-FAR} + \frac{1}{POD} - 1}$	1	0.41

[a] Notation: n represents the number of samples; S_n represents the simulated snowfall; G_n represents the gauge-based snowfall; σ_G represents the standard deviations of gauge snowfall; σ_S represents the standard deviations of simulated snowfall; n_{11} represents the snowfall observed by gauge and reflected by the simulation simultaneously; n_{01} represents snowfall that is not reflected by the simulation but observed by gauge; and n_{10} represents snowfall reflected by the simulation but not observed by gauge. Note that there are events that snowfall is observed neither by gauge nor reflected by the simulation.

Table 12

Comparisons of proportional contributions of snow and glacier meltwater to the total basin discharge from published studies and our work.

Relevant studies	Study area	Model	Period	Meltwater contribution
Our study	Headwaters of the Yangtze River above Zhimenda gauging station	CREST model coupled with a degree-day snow and glacier melt module	2003–2014	Snow: 6.6% Glacier: 5.2%
Zhang et al., 2013	Above Zhimenda gauging station	VIC coupled with a degree-day glacier-melt scheme	1963–2005	Snow: 22.2% Glacier: 6.5%
Wang et al., 2015	Tuotuo River basin	A degree-day model	2000–2012	Snow: 6.8%
Zhang et al., 2008	Tuotuo River basin	A modified degree-day model	1968–2004	Glacier: 32%
Shen et al., 2009	Above Zhimenda gauging station	–	1961–2000	Glacier: 9%

proportional contributions of snow and glacier meltwater to total basin discharge were 22.2% and 6.5%, respectively, during 1963–2005. Wang et al. (2015) employed a degree-day model to estimate a proportional contribution of 6.8% for snow meltwater to total runoff in the Tuotuo River basin during 2000–2012. The Tuotuo River basin is a subbasin of the HRYR, which is closer to the source of the river. These results from different studies vary to some degree, and our result for the snowmelt contribution is much lower than the result of 22.2% by Zhang et al. (2013), but close to that of 6.8% from Wang et al. (2015).

Concerning the glacier meltwater contribution, there are also appreciable differences in the results from published studies. Zhang et al. (2008) found that the contribution was approximately 32% for the period during 1968–2004, using a modified degree-day model for the Tuotuo River basin. Shen et al. (2009) calculated the proportional contribution of glacier meltwater to total basin discharge, obtaining a result of 9% during 1961–2000 in the source region of the Yangtze River. Overall, our results for the contributions of snow and glacier meltwater to total basin discharge appear to be comparable with published results. Our method enjoys the simplicity and feasibility of simulating meltwater over poorly gauged regions using a straightforward temperature index-based model calibrated with remotely sensed SWE or SCA.

Possible reasons for the differences in contributions of meltwater to total runoff are summarized as follows. First, the differences may be associated with different study periods. In our study, a simulation over 2003–2014 was carried out, whereas other studies went back even to the 1960s. Different study periods may lead to different meltwater contributions, as the melting rates and total runoff have been changing over time. Second, the differences may be associated with different focused areas. Different subbasins (i.e., near or far from the source region) may result in different estimates of meltwater contributions. The contributions of meltwater to total runoff may increase as the study area gets closer to the source of the river. Third, the differences may be associated with uncertainties introduced by the model and forcing datasets, such as precipitation. The models applied in previous studies and our study are different from each other, and these models may have many sources of uncertainty (Hughes et al., 2010).

For example, the parameters of the VIC model employed by Zhang et al. (2013) were user specified, and the snowmelt module was not calibrated using observed information on snowfall. On the other hand, the snowmelt module in Wang et al. (2015) is similar to our model with MODIS SCA as the calibration reference, and derived similar contributions of snowmelt to total runoff (i.e., 6.8 and 6.6%, respectively). Therefore, uncertainty resulting from parameters and models does exist in these studies. In addition, Weiland et al. (2015) found that errors in precipitation data may lead to significant uncertainty rather than parameter uncertainty in hydrological modeling, and consequently uncertainty in the snowmelt contributions. Fourth, the differences may be associated with different definitions of snowmelt runoff. In our study, the snowmelt module can be regarded as one-layer model and the snowmelt runoff is surface runoff produced from melting snow. In the two-layer snow accumulation and ablation model that was incorporated into VIC by Zhang et al. (2013), the thin surface layer was used to solve the surface energy balance, and the bottom or pack layer

was used to simulate deeper snowpack (Lu et al., 2018). The definition of snowmelt runoff may therefore be different and result in different snowmelt contributions.

Overall, CREST-snow used in our study performed well in terms of the general consistency between the simulated and remotely sensed snow products. Nevertheless, the glacier melt module is not well suited for application to headwater regions, where the glacier-mass change signal is not dominated in surface water storage changes, and an increasing TWS occurs due to increased precipitation. In this case, parameters associated with glacier melt could be derived from surrounding basins where the glacier-mass change accounts for the major portion of the TWS change as per GRACE. The hydrological model still requires further refinement to become more complete in terms of simulating hydrological state variables, such as groundwater and its interactions with soil moisture and surface water. It is expected that as CREST-snow and remotely sensed products improve, the discrepancies between the simulations and retrievals from multiple satellite missions will be further reduced.

6. Conclusion

In this study, we employed a distributed hydrological model coupled with a snowmelt module (CREST-snow), and PMW SWE and MODIS SCA were taken as the calibration references, achieving NSEs of 0.56 and 0.60, respectively. Snowmelt simulations under two calibration scenarios were mostly consistent, showing contributions of snowmelt to total runoff of 6.7 and 6.5%, respectively. This indicates the overall reliability of snowmelt simulations based on the EHC concept. Results of total runoff simulations showed that CREST-snow performed well for the headwater region, with NSE of 0.82 over 2003–2014. Snow and glacier meltwater contributed ~7 and ~5% to total basin discharge, respectively.

Overall, we developed an effective and practical approach to properly evaluate snowmelt runoff in poorly gauged and ungauged regions based on the EHC. The performance of the snowmelt simulation is expected to improve with increasing spatial resolution and accuracy of PMW SWE. The proposed method can serve as a basis for quantifying proportional contributions of snow and glacier meltwater to total basin discharge for other similar regions globally. The results of this study indicate the possibility of projecting future snowmelt processes and runoff in high mountain regions using CREST-snow, and could be valuable in achieving better water resources management and ecosystem protection across the HRYR and its downstream areas.

Appendix A. Supplementary data

Supplementary data to this article can be found online at https://doi.org/10.1016/j.rse.2019.01.041.

References

Arnell, N.W., Gosling, S.N., 2016. The impacts of climate change on river flood risk at the global scale. Clim. Chang. 134, 387–401.

Ashouri, H., Hsu, K.-L., Sorooshian, S., Braithwaite, D.K., Knapp, K.R., Cecil, L.D., Nelson, B.R., Prat, O.P., 2015. PERSIANN-CDR: daily precipitation climate data record from multisatellite observations for hydrological and climate studies. Bull. Am. Meteorol. Soc. 96, 69–83.

Barnett, T.P., Adam, J.C., Lettenmaier, D.P., 2005. Potential impacts of a warming climate on water availability in snow-dominated regions. Nature 438, 303.

Chao, N., Wang, Z., Hwang, C., Jin, T., Cheng, Y.-S., 2017. Decline of Geladandong Glacier elevation in Yangtze River's source region: detection by ICESat and assessment by hydroclimatic data. Remote Sens. 9, 75.

Che, T., Li, X., Jin, R., Armstrong, R., Zhang, T., 2008. Snow depth derived from passive microwave remote-sensing data in China. Ann. Glaciol. 49, 145–154.

Chen, X., Long, D., Hong, Y., Liang, S., Hou, A., 2017a. Observed radiative cooling over the Tibetan Plateau for the past three decades driven by snow cover-induced surface albedo anomaly. J. Geophys. Res.-Atmos. 122 (12), 6170–6185.

Chen, X., Long, D., Hong, Y., Zeng, C., Yan, D., 2017b. Improved modeling of snow and glacier melting by a progressive two-stage calibration strategy with GRACE and multisource data: how snow and glacier meltwater contributes to the runoff of the Upper Brahmaputra River basin? Water Resour. Res. 53, 2431–2466.

Chen, X., Long, D., Liang, S., He, L., Zeng, C., Hao, X., Hong, Y., 2018. Developing a composite daily snow cover extent record over the Tibetan Plateau from 1981 to 2016 using multisource data. Remote Sens. Environ. 215, 284–299.

Dai, L., Che, T., Wang, J., Zhang, P., 2012. Snow depth and snow water equivalent estimation from AMSR-E data based on a priori snow characteristics in Xinjiang, China. Remote Sens. Environ. 127, 14–29.

Dai, L., Che, T., Ding, Y., 2015. Inter-calibrating SMMR, SSM/I and SSMI/S data to improve the consistency of snow-depth products in China. Remote Sens. 7, 7212–7230.

Dai, L.Y., Che, T., Ding, Y.J., Hao, X.H., 2017. Evaluation of snow cover and snow depth on the Qinghai-Tibetan Plateau derived from passive microwave remote sensing. Cryosphere 11, 1933–1948.

Dai, L.Y., Che, T., Xie, H., Wu, X., 2018. Estimation of snow depth over the Qinghai-Tibetan Plateau based on AMSR-E and MODIS data. Remote Sens. 10 (12), 1989.

Ding, B., Yang, K., Qin, J., Wang, L., Chen, Y., He, X., 2014. The dependence of precipitation types on surface elevation and meteorological conditions and its parameterization. J. Hydrol. 513, 154–163.

Dong, J., Walker, J.P., Houser, P.R., 2005. Factors affecting remotely sensed snow water equivalent uncertainty. Remote Sens. Environ. 97 (1), 68–82.

Dressler, K., Leavesley, G., Bales, R., Fassnacht, S., 2006. Evaluation of gridded snow water equivalent and satellite snow cover products for mountain basins in a hydrologic model. Hydrol. Process. 20, 673–688.

Dudhia, J., Hong, S.Y., Lim, K.S., 2008. A new method for representing mixed-phase particle fall speeds in bulk microphysics parameterizations. J. Meteorol. Soc. Jpn. Ser. II 86, 33–44.

Ebert, E.E., Janowiak, J.E., Kidd, C., 2007. Comparison of near-real-time precipitation estimates from satellite observations and numerical models. Bull. Am. Meteorol. Soc. 88 (1), 47–64.

Engineers, U. A. C. O., 1956. Snow Hydrology: Summary Report of the Snow Investigations. US Army of Engineers North Pacific Division.

Famiglietti, J., Cazenave, A., Eicker, A., Reager, J., Rodell, M., Velicogna, I., 2015. Satellites provide the big picture. Science 349, 684–685.

Ferguson, R., 1999. Snowmelt runoff models. Prog. Phys. Geogr. 23, 205–227.

Fontaine, T., Cruickshank, T., Arnold, J., Hotchkiss, R., 2002. Development of a snowfall–snowmelt routine for mountainous terrain for the soil water assessment tool (SWAT). J. Hydrol. 262, 209–223.

Foster, J.L., Sun, C.J., Walker, J.P., Kelly, R., Chang, A., Dong, J.R., Powell, H., 2005. Quantifying the uncertainty in passive microwave snow water equivalent observations. Remote Sens. Environ. 94, 187–203.

Guo, W., Liu, S., Xu, J., Wu, L., Shangguan, D., Yao, X., Wei, J., Bao, W., Yu, P., Liu, Q., 2015. The second Chinese glacier inventory: data, methods and results. J. Glaciol. 61, 357–372.

Hall, D.K., Riggs, G.A., 2007. Accuracy assessment of the MODIS snow products. Hydrol. Process. 21, 1534–1547.

Hall, D., Riggs, G., Salomonson, V., 2006. MODIS/Terra Snow Cover 8-day L3 Global 500m Grid V005. National Snow and Ice Data Center, Colorado USA.

Hall, D., Riggs, G., Salomonson, V., 2007. MODIS/Aqua snow cover 8-day L3 global 500m grid, version 5. National Snow and Ice Data Center, Boulder, CO digital media. Available online at. http://nsidc.org/data/myd10a2v5.html.

Hay, L.E., Clark, M.P., Wilby, R.L., Gutowski Jr., W.J., Leavesley, G.H., Pan, Z., Arritt, R.W., Takle, E.S., 2002. Use of regional climate model output for hydrologic simulations. J. Hydrometeorol. 3, 571–590.

Henn, B., Painter, T.H., Bormann, K.J., McGurk, B., Flint, A.L., Flint, L.E., ... Lundquist, J.D., 2018. High-elevation evapotranspiration estimates during drought: using streamflow and NASA airborne snow observatory SWE observations to close the Upper Tuolumne River Basin water balance. Water Resour. Res. 54 (2), 746–766.

Hensley, S., Rosen, P.A., Gurrola, E., 2000. Topographic map generation from the Shuttle Radar Topography Mission C-band SCANSAR interferometry. In: Microwave Remote Sensing of the Atmosphere and Environment II. International Society for Optics and Photonics, pp. 179–190.

Huang, Q., Long, D., Du, M., Zeng, C., Li, X., Hou, A., Hong, Y., 2018a. An improved approach to monitoring Brahmaputra River water levels using retracked altimetry data. Remote Sens. Environ. 211, 112–128.

Huang, Q., Long, D., Du, M., Zeng, C., Qiao, G., Li, X., ... Hong, Y., 2018b. Discharge estimation in high-mountain regions with improved methods using multisource remote sensing: a case study of the Upper Brahmaputra River. Remote Sens. Environ. 219, 115–134.

Huffman, G.J., Adler, R.F., Bolvin, D.T., Gu, G.J., Nelkin, E.J., Bowman, K.P., Hong, Y., Stocker, E.F., Wolff, D.B., 2007. The TRMM multisatellite precipitation analysis (TMPA): quasi-global, multiyear, combined-sensor precipitation estimates at fine scales. J. Hydrometeorol. 8, 38–55.

Hughes, D., Kapangaziwiri, E., Sawunyama, T., 2010. Hydrological model uncertainty assessment in southern Africa. J. Hydrol. 387, 221–232.

Hutchinson, M.F., 1995. Interpolating mean rainfall using thin plate smoothing splines. Int. J. Geogr. Inf. Syst. 9 (4), 385–403.

Ikeda, K., Rasmussen, R., Liu, C., Gochis, D., Yates, D., Chen, F., ... Arsenault, K., 2010. Simulation of seasonal snowfall over Colorado. Atmos. Res. 97 (4), 462–477.

Immerzeel, W.W., 2008. Spatial modeling of mountainous basins: An integrated analysis of the hydrological cycle, climate change and agriculture. In: Netherlands Geographical Studies. vol. 369 KNAG, Utrecht.

Immerzeel, W.W., Droogers, P., de Jong, S.M., Bierkens, M.F.P., 2009. Large-scale monitoring of snow cover and runoff simulation in Himalayan river basins using remote sensing. Remote Sens. Environ. 113, 40–49.

Immerzeel, W.W., Van Beek, L.P., Bierkens, M.F., 2010. Climate change will affect the Asian water towers. Science 328, 1382–1385.

Jiang, T., Su, B., Hartmann, H., 2007. Temporal and spatial trends of precipitation and river flow in the Yangtze River Basin, 1961–2000. Geomorphology 85, 143–154.

Joyce, R.J., Janowiak, J.E., Arkin, P.A., Xie, P., 2004. CMORPH: a method that produces global precipitation estimates from passive microwave and infrared data at high spatial and temporal resolution. J. Hydrometeorol. 5, 487–503.

Kang, S., Wang, F., Morgenstern, U., Zhang, Y., Grigholm, B., Kaspari, S., Schwikowski, M., Ren, J., Yao, T., Qin, D., 2015. Dramatic loss of glacier accumulation area on the Tibetan Plateau revealed by ice core tritium and mercury records. Cryosphere 9, 1213–1222.

Khan, S.I., Adhikari, P., Hong, Y., Vergara, H., Grout, T., Adler, R.F., Policelli, F., Irwin, D., Korme, T., Okello, L., 2010. Observed and simulated hydroclimatology using distributed hydrologic model from in-situ and multi-satellite remote sensing datasets in Lake Victoria region in East Africa. Hydrol. Earth Syst. Sci. Discuss. 7, 4785–4816.

Khan, S.I., Hong, Y., Wang, J., Yilmaz, K.K., Gourley, J.J., Adler, R.F., Brakenridge, G.R., Policelli, F., Habib, S., Irwin, D., 2011. Satellite remote sensing and hydrologic modeling for flood inundation mapping in Lake Victoria basin: implications for hydrologic prediction in ungauged basins. IEEE Trans. Geosci. Remote Sens. 49, 85–95.

Klemes, V., 1990. The modelling of mountain hydrology: the ultimate challenge. IAHS Publ. 190, 29–43.

Latif, Y., Yaoming, M., Yaseen, M., 2018. Spatial analysis of precipitation time series over the Upper Indus Basin. Theor. Appl. Climatol. 131, 761–775.

Li, L., Dai, S., Shen, H., Li, H., Xiao, J., 2012. Response of water resources to climate change and its future trend in the source region of the Yangtze River. Acta Geograph. Sin. 67, 941–950.

Li, H., Tang, Z., Wang, J., Che, T., Pan, X., Huang, C., Wang, X., Hao, X., Sun, S., 2014. Synthesis method for simulating snow distribution utilizing remotely sensed data for the Tibetan Plateau. J. Appl. Remote Sens. 8, 084696.

Lindsay, R., Wensnahan, M., Schweiger, A., Zhang, J., 2014. Evaluation of seven different atmospheric reanalysis products in the Arctic. J. Clim. 27, 2588–2606.

Long, D., Shen, Y., Sun, A., Hong, Y., Longuevergne, L., Yang, Y., ... Chen, L., 2014. Drought and flood monitoring for a large karst plateau in Southwest China using extended GRACE data. Remote Sens. Environ. 155, 145–160.

Long, D., Yang, Y., Wada, Y., Hong, Y., Liang, W., Chen, Y., ... Chen, L., 2015. Deriving scaling factors using a global hydrological model to restore GRACE total water storage changes for China's Yangtze River Basin. Remote Sens. Environ. 168, 177–193.

Long, D., Chen, X., Scanlon, B.R., Wada, Y., Hong, Y., Singh, V.P., ... Yang, W., 2016. Have GRACE satellites overestimated groundwater depletion in the Northwest India Aquifer? Sci. Rep. 6, 24398.

Long, D., Pan, Y., Zhou, J., Chen, Y., Hou, X., Hong, Y., Scanlon, B.R., Longuevergne, L., 2017. Global analysis of spatiotemporal variability in merged total water storage changes using multiple GRACE products and global hydrological models. Remote Sens. Environ. 192, 198–216.

Lu, W., Wang, W., Shao, Q., Yu, Z., Hao, Z., Xing, W., ... Li, J., 2018. Hydrological projections of future climate change over the source region of Yellow River and Yangtze River in the Tibetan Plateau: a comprehensive assessment by coupling RegCM4 and VIC model. Hydrol. Process. 32 (13), 2096–2117.

Lundquist, J.D., Chickadel, C., Cristea, N., Currier, W.R., Henn, B., Keenan, E., Dozier, J., 2018. Separating snow and forest temperatures with thermal infrared remote sensing. Remote Sens. Environ. 209, 764–779.

McCabe, M.F., Wood, E.F., Wojcik, R., Pan, M., Sheffield, J., Gao, H., Su, H., 2008. Hydrological consistency using multi-sensor remote sensing data for water and energy cycle studies. Remote Sens. Environ. 112, 430–444.

McKay, G., Thompson, H., 1968. Snowcover in the prairie provinces of Canada. Trans. ASAE 11, 812–0815.

McVicar, T.R., Roderick, M.L., Donohue, R.J., Li, L.T., Van Niel, T.G., Thomas, A., Grieser, J., Jhajharia, D., Himri, Y., Mahowald, N.M., Mescherskaya, A.V., Kruger, A.C., Rehman, S., Dinpashoh, Y., 2012. Global review and synthesis of trends in observed terrestrial near-surface wind speeds: implications for evaporation. J. Hydrol. 416-417, 182–205.

Mostovoy, G.V., King, R.L., Reddy, K.R., Kakani, V.G., Filippova, M.G., 2006. Statistical estimation of daily maximum and minimum air temperatures from MODIS LST data over the state of Mississippi. GISci. Remote Sens. 43, 78–110.

Nash, J. Eamonn, Sutcliffe, Jonh V., 1970. River flow forecasting through conceptual models part I—a discussion of principles. J. Hydrol. 10 (3), 282–290.

Neteler, M., 2010. Estimating daily land surface temperatures in mountainous environments by reconstructed MODIS LST data. Remote Sens. 2, 333–351.

Pachauri, R.K., Allen, M.R., Barros, V.R., Broome, J., Cramer, W., Christ, R., Church, J.A., Clarke, L., Dahe, Q., Dasgupta, P., 2014. Climate change 2014: synthesis report. In: Contribution of Working Groups I, II and III to the Fifth Assessment Report of the Intergovernmental Panel on Climate Change. IPCC.

Palmer, J., 2017. Chile's glacial lakes pose newly recognized flood threat. Science (New York, N.Y.) 355 (6329), 1004–1005.

Parajka, J., Blöschl, G., 2008. The value of MODIS snow cover data in validating and calibrating conceptual hydrologic models. J. Hydrol. 358, 240–258.

Pietroniro, A., Prowse, T.D., 2002. Applications of remote sensing in hydrology. Hydrol. Process. 16, 1537–1541.

Qin, D.H., Liu, S.Y., Li, P.J., 2006. Snow cover distribution, variability, and response to climate change in western China. J. Clim. 19, 1820–1833.

Rasmussen, R., Liu, C., Ikeda, K., Gochis, D., Yates, D., Chen, F., ... Miller, K., 2011. High-resolution coupled climate runoff simulations of seasonal snowfall over Colorado: a process study of current and warmer climate. J. Clim. 24 (12), 3015–3048.

Romshoo, S.A., Dar, R.A., Rashid, I., Marazi, A., Ali, N., Zaz, S.N., 2015. Implications of shrinking cryosphere under changing climate on the streamflows in the Lidder catchment in the Upper Indus Basin, India. Arct. Antarct. Alp. Res. 47, 627–644.

Savoie, M.H., Armstrong, R.L., Brodzik, M.J., Wang, J.R., 2009. Atmospheric corrections for improved satellite passive microwave snow cover retrievals over the Tibet Plateau. Remote Sens. Environ. 113 (12), 2661–2669.

Schmugge, T.J., Kustas, W.P., Ritchie, J.C., Jackson, T.J., Rango, A., 2002. Remote sensing in hydrology. Adv. Water Resour. 25, 1367–1385.

Seligman, G., Douglas, C., 1936. Snow Structure and Ski Fields. Macmillan.

Shen, Y., Xiong, A.Y., 2016. Validation and comparison of a new gauge-based precipitation analysis over mainland China. Int. J. Climatol. 36, 252–265.

Shen, Y., Wang, G., Wang, G., Pu, J., Wang, X., 2009. Impacts of climate change on glacial water resources and hydrological cycles in the Yangtze River source region, the Qinghai-Tibetan Plateau, China: a progress report. Sci. Cold Arid Reg. 1, 0475–0495.

Shen, X., Hong, Y., Zhang, K., Hao, Z., 2016. Refining a distributed linear reservoir routing method to improve performance of the CREST model. J. Hydrol. Eng. 22, 04016061.

Shrestha, M., Koike, T., Hirabayashi, Y., Xue, Y., Wang, L., Rasul, G., Ahmad, B., 2015. Integrated simulation of snow and glacier melt in water and energy balance-based, distributed hydrological modeling framework at Hunza River Basin of Pakistan Karakoram region. J. Geophys. Res.-Atmos. 120, 4889–4919.

Singh, P., Kumar, N., 1997. Impact assessment of climate change on the hydrological response of a snow and glacier melt runoff dominated Himalayan river. J. Hydrol. 193, 316–350.

Sorg, A., Bolch, T., Stoffel, M., Solomina, O., Beniston, M., 2012. Climate change impacts on glaciers and runoff in Tien Shan (Central Asia). Nat. Clim. Chang. 2, 725–731.

Sun, G., Deng, W., Shao, Q., Hua, R., 1992. Textual research on the main source of the Changjiang river. Chin. Geogr. Sci. 90–98.

Tang, G., Ma, Y., Long, D., Zhong, L., Hong, Y., 2016. Evaluation of GPM Day-1 IMERG and TMPA Version-7 legacy products over Mainland China at multiple spatio-temporal scales. J. Hydrol. 533, 152–167.

Tang, G., Wen, Y., Gao, J., Long, D., Ma, Y., Wan, W., Hong, Y., 2017. Similarities and differences between three coexisting spaceborne radars in global rainfall and snowfall estimation. Water Resour. Res. 53 (5), 3835–3853.

Tang, G., Behrangi, A., Long, D., Li, C., Hong, Y., 2018a. Accounting for spatiotemporal errors of gauges: a critical step to evaluate gridded precipitation products. J. Hydrol. 559, 294–306.

Tang, G., Long, D., Hong, Y., Gao, J., Wan, W., 2018b. Documentation of multifactorial

relationships between precipitation and topography of the Tibetan Plateau using spaceborne precipitation radars. Remote Sens. Environ. 208, 82–96.

Viviroli, D., Weingartner, R., 2004. The hydrological significance of mountains: from regional to global scale. Hydrol. Earth Syst. Sci. Discuss. 8, 1017–1030.

Wang, G.-x., Li, Y.-s., Wang, Y.-b., Shen, Y.-p., 2007. Impacts of Alpine Ecosystem and Climate Changes on Surface Runoff in the Headwaters of the Yangtze River.

Wang, B., Bao, Q., Hoskins, B., Wu, G., Liu, Y., 2008. Tibetan Plateau warming and precipitation changes in East Asia. Geophys. Res. Lett. 35.

Wang, J., Hong, Y., Li, L., Gourley, J.J., Khan, S.I., Yilmaz, K.K., Adler, R.F., Policelli, F.S., Habib, S., Irwn, D., 2011. The coupled routing and excess storage (CREST) distributed hydrological model. Hydrol. Sci. J. 56, 84–98.

Wang, R., Yao, Z., Liu, Z., Wu, S., Jiang, L., Wang, L., 2015. Snow cover variability and snowmelt in a high-altitude ungauged catchment. Hydrol. Process. 29, 3665–3676.

Wang, Y., Zhang, Y., Chiew, F.H., McVicar, T.R., Zhang, L., Li, H., Qin, G., 2017. Contrasting runoff trends between dry and wet parts of eastern Tibetan Plateau. Sci. Rep. 7, 15458.

Wei, J., Liu, S., Guo, W., Yao, X., Xu, J., Bao, W., Jiang, Z., 2014. Surface-area changes of glaciers in the Tibetan Plateau interior area since the 1970s using recent Landsat images and historical maps. Ann. Glaciol. 55, 213–222.

Weiland, F.C.S., Vrugt, J.A., Weerts, A.H., Bierkens, M.F., 2015. Significant uncertainty in global scale hydrological modeling from precipitation data errors. J. Hydrol. 529, 1095–1115.

Wild, M., 2009. Global dimming and brightening: a review. J. Geophys. Res. 114.

Willett, K.M., Jones, P.D., Gillett, N.P., Thorne, P.W., 2008. Recent changes in surface humidity: development of the HadCRUH dataset. J. Clim. 21, 5364–5383.

Xiao, X., Zhang, T., Zhong, X., Shao, W., Li, X., 2018. Support vector regression snow-depth retrieval algorithm using passive microwave remote sensing data. Remote Sens. Environ. 210, 48–64.

Xue, X., Hong, Y., Limaye, A.S., Gourley, J.J., Huffman, G.J., Khan, S.I., Dorji, C., Chen, S., 2013. Statistical and hydrological evaluation of TRMM-based multi-satellite precipitation analysis over the Wangchu Basin of Bhutan: are the latest satellite precipitation products 3B42V7 ready for use in ungauged basins? J. Hydrol. 499, 91–99.

Yang, J.P., Ding, Y.J., Shen, Y.P., Liu, S.Y., Chen, R.S., 2004. Climatic features of eco-environment change in the source regions of the Yangtze and Yellow Rivers in recent 40 years. J. Glaciol. Geocryol. 1 (002).

Zappa, M., Pos, F., Strasser, U., Warmerdam, P., Gurtz, J., 2003. Seasonal water balance of an Alpine catchment as evaluated by different methods for spatially distributed snowmelt modelling. Hydrol. Res. 34, 179–202.

Zeng, C., Shen, H., Zhong, M., Zhang, L., Wu, P., 2015. Reconstructing MODIS LST based on multitemporal classification and robust regression. IEEE Geosci. Remote Sens. Lett. 12 (3), 512–516.

Zhang, Y., Liu, S., Xu, J., Shangguan, D., 2008. Glacier change and glacier runoff variation in the Tuotuo River basin, the source region of Yangtze River in western China. Environ. Geol. 56, 59–68.

Zhang, G., Xie, H., Yao, T., Liang, T., Kang, S., 2012. Snow cover dynamics of four lake basins over Tibetan Plateau using time series MODIS data (2001 − 2010). Water Resour. Res. 48 (10).

Zhang, S., Ye, B., Liu, S., Zhang, X., Hagemann, S., 2012. A modified monthly degree-day model for evaluating glacier runoff changes in China. Part I: model development. Hydrol. Process. 26, 1686–1696.

Zhang, L., Su, F., Yang, D., Hao, Z., Tong, K., 2013. Discharge regime and simulation for the upstream of major rivers over Tibetan Plateau. J. Geophys. Res.-Atmos. 118, 8500–8518.

Zhang, Y., Xie, H., Yao, T., Li, H., Duan, S., 2014. Quantitative water resources assessment of Qinghai Lake basin using Snowmelt Runoff Model (SRM). J. Hydrol. 519, 976–987.

Zhang, Y., Hong, Y., Wang, X., Gourley, J.J., Xue, X., Saharia, M., Ni, G., Wang, G., Huang, Y., Chen, S., Tang, G., 2015. Hydrometeorological analysis and remote sensing of extremes: was the July 2012 Beijing flood event detectable and predictable by global satellite observing and global weather modeling systems? J. Hydrometeorol. 16, 381–395.